Taylor & Francis
Taylor & Francis Group

CHEMISTRY AND MINERALOGY OF TITANIA-RICH SLAGS. PART 1—HEMO-ILMENITE, SULPHATE, AND UPGRADED TITANIA SLAGS

MICHEL GUÉGUIN
FRANÇOIS CARDARELLI

Technology Department, Rio Tinto Iron and Titanium, Inc., Sorel Tracy, Quebec, Canada

Titania-rich slags with 80 mass percent TiO_2 are produced in the electric arc furnaces of QIT-Fer & Titane, Inc., by the continuous smelting of hemo-ilmenite ore with anthracite coal. Titania slag represents an important feedstock for the manufacture of titanium dioxide pigment by the sulphate process. Moreover, part of the production of the titania-rich slag is further acid-leached under a high-pressure and moderate-temperature hydrometallurgical process to yield an upgraded titania slag with 94.5 mass percent TiO_2, which is used in the chloride process. After describing in detail the beneficiation, chemistry, and mineralogy of the hemo-ilmenite ore, this article reviews the unique crystallochemistry and mineralogy of the titanate phases with pseudobrookite-karrooite structure and to a lesser extent silicates and oxides present in these titania-rich feedstocks, focusing on the chemical reactions occurring at each step of the pyro- and hydro-metallurgical processes. The behavior of major elements such as titanium, iron, magnesium, calcium, aluminum, and silicon along with that of minor elements such as vanadium, chromium, and manganese are particularly detailed. A general discussion of the methods specifically developed for the

Address correspondence to F. Cardarelli, Technology Department, Rio Tinto Iron and Titanium, Inc., 1625 Route Marie-Victorin, Sorel Tracy, QC J3R 1M6, Canada. E-mail: francois.cardarelli@rtit.com

study of the synthetic minerals present in these materials is also presented.

INTRODUCTION

Since 1950, the nameplate production capacity of titania-rich slag at the metallurgical complex of QIT-Fer & Titane Inc. (formerly named Quebec Iron & Titanium and later referred in the text as QIT), located in Sorel Tracy, Province of Quebec, Canada, ramped up from 250,000 t up to about 1,100,000 t. The titania-rich slag with 80 mass percent TiO_2 is produced by the continuous smelting of hemo-ilmenite ore with anthracite coal in an electric arc furnace (EAF). The hard rock hemo-ilmenite ore is mined from the anorthositic Lac Tio deposit, Allard Lake, Quebec, Canada (Hammond 1952). Part of the production of the crude titania-rich slag is used as feedstock for the manufacture of titanium dioxide pigment by the sulphate process. The molten iron coproduced during the slagging process is either sold as pig iron or converted into steel or even atomized into iron or steel powders, respectively. Another part of the production of the crude titania-rich slag is further acid-leached under a high-pressure and moderate-temperature hydrometallurgical process to yield an upgraded titania slag with 94.5 mass percent TiO_2. The chemistry and mineralogy of these synthetic titania-rich feedstock's is unique among other industrial products and relatively complex due to several factors. 1) the high titania content of the metallurgical slag produced leads to the formation of synthetic mineral species, mainly titanates that occur quite exclusively in extraterrestrial materials (e.g., lunar regolith, meteorites) and only extremely rarely in geological or in man-made materials. 2) The chemistry of the existing phases is always subject to departure from the theoretical composition due to important isomorphic substitutions between major and minor metals. Finally, 3) the harsh physical and chemical treatments performed at each step of the process favors the formation of metastable phases. The studies and results presented in this article summarize more than 35 years of research investigations conducted the first author at QIT-Fer & Titane, Inc. These results have led to major improvements of the existing process and to a great enhancement of the quality of the titania-rich slags since the first implementation in 1950 of the slagging process by the Kennecott Copper and New Jersey Zinc companies (Peirce et al. 1949).

EXPERIMENTAL

The various types of experimental methods used during the investigation are described in the following paragraphs.

Samples Preparation

The various titania-rich products were sampled in the field at the QIT plant and were in the form of crushed chunks (e.g., hemo-ilmenite ore, ore concentrate), lumps or blocks (e.g., titania-rich slag), or sized particles (e.g., Sorelslag, reduced slag, oxidized slag, heat-treated slag, and upgraded titania slag). For the microscopic examination, the material was crushed with a small jaw-crusher and mounted into epoxy resin to produce polished sections. For chemical analysis, all the crushed samples were also ground into a disk grinder with a hard metal (WC-Co) lining (Fritsch) until the size was below 325 mesh.

Synthetic Minerals Separation

Because of the intricate nature of titanate phases occurring in titania-rich slags along with the presence of other numerous minor minerals and synthetic species, an important part of the experimental work first consisted of separating and concentrating the various natural and synthetic solid compounds occurring in the product after each step of the QIT processing. For achieving such a tedious task, it was necessary to select the most efficient and reliable physical separation method. By contrast with other natural ores and products found extensively in the mining and metallurgical industry, mostly composed of oxides, carbonates, silicates, sulphides, and phosphates minerals species that can be easily separated by density, the gravimetric separation of the titanates and oxides phases in titania-rich slags by the sink-float method does not provide an efficient technique from an analytical point of view. Actually, most titanates, oxides, and sulphides occurring in titania-rich slags exhibit a high density, usually well above that of common heavy liquids used in the mineralogical laboratory and the close vicinity of their respective densities further impedes a sharp separation between different phases. For instance, the densities of most titanates, oxides, and sulphides identified in titania-rich slags are listed in Table 1, along with the cut-off limits of the most common heavy liquids used in the mineral dressing laboratory.

Table 1. Minerals in titania-rich slag ordered by decreasing mass densities

Mineral species	Classification according to mineral density
Iron	Highly dense minerals fraction (4150 $kg \cdot m^{-3} < d < 8000\ kg \cdot m^{-3}$)
Cobaltite	
Millerite	
Haematite	
Magnetite	
Troilite	
Anosovite	
Linnaeite	
Siegenite	
Ilmenite	
Ulvospinel	
Pyrophanite	
Magnesioferrite	
Berdesinskiite	
Schreyerite	
Olkhonskite	
Pseudobrookite	
Rutile	
Hercynite	
Brookite	

Clerici's solution (Thallium malonate and formate) 4150 $kg \cdot m^{-3}$

Perovskite	Dense minerals fraction (3125 $kg \cdot m^{-3} < d < 4150\ kg \cdot m^{-3}$)
Qandilite	
Pseudorutile	
Chalcopyrite	
Pyrrhotite	
Armalcolite	
Anatase	
Geikielite	
Kyzylkumite	
Tialite	
Spinel	

Diiodomethane (3125 $kg \cdot m^{-3}$)
Tetrabromoethane (2960 $kg \cdot m^{-3}$)

Phlogopite	Light minerals fraction ($d < 2890\ kg \cdot m^{-3}$)
Plagioclase	
Titanite	

Bromoform (2860 $kg \cdot m^{-3}$)

Note: Minerals in bold type are those identified in QIT products.

Close examination of Table 1 shows clearly that using common halogenated heavy liquids such as bromoform ($2860 \, \text{kg} \cdot \text{m}^{-3}$), 1,1,2,2-tetrabromoethane ($2960 \, \text{kg} \cdot \text{m}^{-3}$) or even the denser diiodomethane ($3125 \, \text{kg} \cdot \text{m}^{-3}$) only allows us to separate the titanates, oxides, and sulphides phases from minor silicates minerals from the gangue. But even the utilization of the hazardous Clerici's solution (i.e., aqueous solution of thallium malonate and formate) is quite inefficient to accurately separate the titanates and to a lesser extent, sulphides and some oxides belonging, to the spinel group. Some past studies conducted on titania-rich slags from QIT (Forman et al. 1954) demonstrate that the sink-float separation using Clerici's solution is not entirely satisfactory from an analytical point of view. Therefore, other types of physical separation were also investigated.

Among other techniques, the magnetic separation was the most efficient, especially when performed on ground titania-rich slags (Guéguin 1972, 2004a). The separation was based on the following facts. 1) many magnesian and ferroan titanates exhibit distinguishable magnetic properties (Lethuillier and Massal 1980; Shirane et al. 1962), some being antiferromagnetic, other, being ferrimagnetic, and others being only paramagnetic or diamagnetic. 2) During some steps of the process, metallic iron nodules are usually surrounded by a rim of iron sulphide and are also coated by a glassy silicate phase. Therefore, the magnetic separation allows us to separate both metallic iron, iron sulphide, and silicates from the titanates in one step (Guéguin 2004b). Hence the magnetic separation allowed to produce a concentrate of titanate phases including scarce titanate phases difficult to distinguish without such methods and that become easy to identify by x-ray diffraction and electron microprobe chemical analysis. In practice, the crushed sample of the product is separated using a Carpco lifting magnet, Model MLH(13)111-5 (Outokumpu Technology, Inc., Jacksonville, FL, USA), at various current intensities with a drum angular velocity of 75 revolutions per min and a 6.0 mm roll-to-block gap setting. The relationship between the circulating current intensity, I, in amperes (A) and the magnetic field induction B in Tesla (T) was established experimentally and exhibits a polynomial form as

$$B = 0.0273 + 0.3159I + 0.1046 \, I^2 - 0.0499 \, I^3 - 0.0053 \, I^4.$$

During the separation operation, each fraction is collected and accurately weighed. The mass fractions are then reported graphically vs. the

magnetic field induction. Two types of plots are currently used: 1) the mass fraction, w, expressed in wt. % as a function of the magnetic field induction, B, in T, $w = f(B)$ and 2) the cumulative mass fractions vs. the magnetic field induction. The two plots are presented in Figures 1 and 2, respectively. For instance, typical x-ray diffractograms performed either on the Sorelslag, as received, after magnetic separation conducted at low and high magnetic field induction are presented in Figures 13 and 14, respectively. From these spectra, it can be clearly seen that the efficiency of the magnetic separation to reveal minor phases (e.g., troilite, anosovite) usually are so dispersed into the material that their examination needs hours of observation under the microscope.

Optical Microscopy Under Reflected Natural and Polarized Light

Representative samples of various materials discussed in this article were selected from bulk samples, embedded into epoxy-resin, and polished to obtain polished sections suitable for microscopic and mineralogical examination under natural reflected light with plane and crossed Nichols
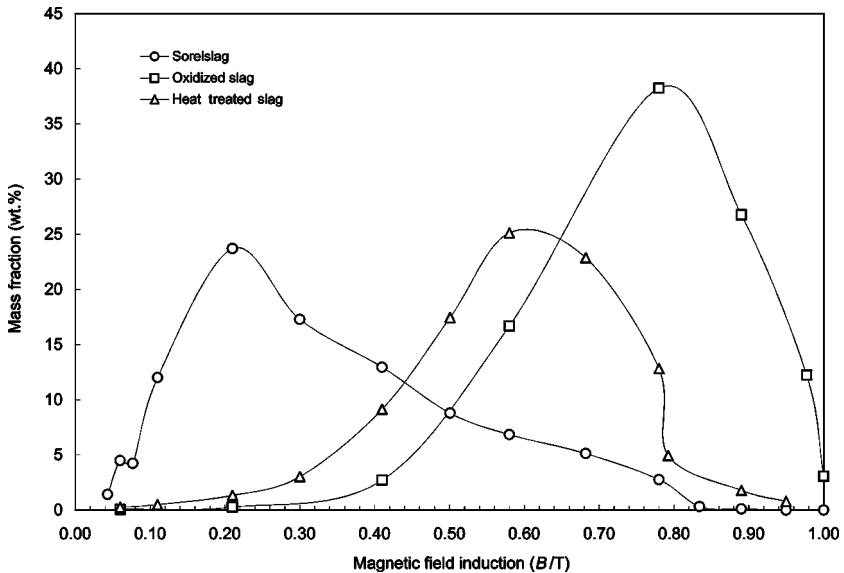
Figure 1. Mass fraction collected vs. magnetic field induction for QIT titania-rich slags.
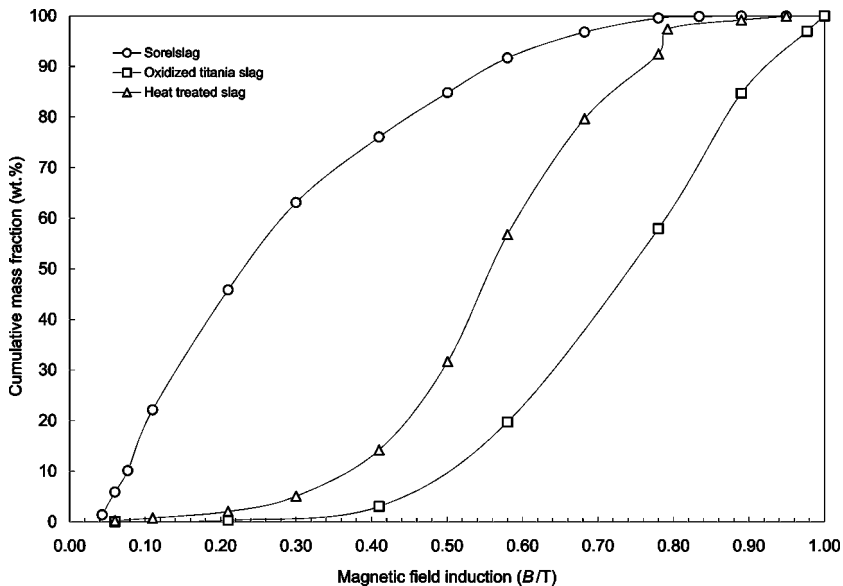
Figure 2. Cumulative mass fraction vs. magnetic field induction for QIT titania-rich slags.

polarized light using a metallographic microscope. These polished section were also coated with a layer of carbon to be observed under scanning electron microscope (SEM).

Electron Probe Microchemical Analysis (EPMA)

The in situ chemical analysis of major, minor, and trace elements was performed using a JEOL 8900 electron microprobe analyzer equipped with a wavelength-dispersive (WDS) system under conditions of 20 kV accelerating voltage and 30 nA sample current. The counting system is equipped with several crystals used as monochromators (Rowland radius = 140 mm) and a gas flow detector. Peak searches were made for Ti, Mg, Fe, Al, Ca, V, Cr, Mn, and Fe for titanates, while peak searches were made for Fe, Cu, Ni, Co, As, Sb, and S in sulphides and sulfosalts, and finally Si, Al, Fe, Mg, Ca, Mn, K, Na, and Ti in silicates.

   Peak search was assisted by pulse-height analysis (PHA) to reduce the background x-ray intensity. The peak intensities were measured over a long counting period (20 s for most elements and 100 s for V) for each spot, using a 1-μm diameter electron beam spot. During the counting,

the sample stage was translated over a square area $(3–4\,\mu m^2)$ for each spot to prevent sample damage. Calibration was conducted using specific standard minerals with definite chemical composition and crystal mono-chromators for each chemical element. The standard deviations and detection limit intensities of each chemical element for titanates, sili-cates, and sulphides are listed in Tables 2–4, respectively.

Note that EPMA does not provide the oxidation states of elements to be analyzed. Moreover, all the empirical chemical formulae of the phases analyzed were normalized with respect to a number of oxygen atoms for oxides, titanates, silicates, and sulphur atoms for sulphides and sulfosalts. The microchemical anlysis along with the calculated empirical formulae of each phase analyzed by EPMA are presented in Table 5 for titanates, in Table 6 for sulphides and sulfosalts, and in Table 7 for silicates.

X-ray Powder Diffraction (XRD)

The qualitative identification of crystallized phases was conducted by powder diffraction using the Bragg–Brentano technique. The diffractometer

Table 2. WDS calibration standards, crystal monochromators, and detection limits for titanates

Chemical element (Symbol)	Standard mineral name	Monochomator crystal acronym	Standard deviation $(SD/\%)$	Detection limit $(w_{DL}/ppm\ wt.)$
Aluminum (Al)	Spinel	TAP	0.22	225
Calcium (Ca)	Diopside	PETJ	0.40	254
Chromium (Cr)	Eskolaite	LiF	0.57	497
Cobalt (Co)	Siegenite	LiF	0.41	508
Iron (Fe)	Magnetite	LiFH	0.19	379
Magnesium (Mg)	Spinel	TAP	0.36	165
Manganese (Mn)	Willemite	LiFH	0.88	308
Nickel (Ni)	Bunsenite	LiFH	0.20	360
Silicon (Si)	Diopside	TAP	0.23	384
Titanium (Ti)	Rutile	LiF	0.55	700
Vanadium (V)	Vanadinite	LiF	1.10	517

Notes: 1) LiF = Lithium fluoride; LiFH = Lithium fluoride; TAP = Thallium acid phta-late; PETJ = Penthaerythritol with Johansson geometry and 2) standard deviation is given for a confidence interval of 95% (i.e., 2σ).

Table 3. WDS calibration standards, crystal monochromators, and detection limits for silicates

Chemical element (Symbol)	Standard mineral name	Monochomator crystal acronym	Standard deviation (SD/%)	Detection limit (w_{DL}/ppm wt.)
Aluminium (Al)	Orthoclase	TAP	0.58	218
Calcium (Ca)	Diopside	PETJ	0.63	296
Chromium (Cr)	Chromite	PETJ	0.68	750
Iron (Fe)	Magnetite	LiFH	0.34	413
Magnesium (Mg)	Diopside	TAP	0.66	215
Manganese (Mn)	Spessartine	LiFH	0.53	396
Potassium (K)	Orthoclase	PETJ	0.76	259
Silicon (Si)	Orthoclase	TAP	0.29	322
Sodium (Na)	Albite	TAP	1.43	306
Titanium (Ti)	Rutile	PETJ	0.43	502

Notes: 1) LiF = Lithium fluoride; LiFH = Lithium fluoride; TAP = Thallium acid phtalate; PETJ = Pentaerythritol with Johansson geometry and 2) standard deviation is given for a confidence interval of 95% (i.e., 2σ).

is the Geigerflex model 8510 from Rigaku (Sendagaya, Japan) with a Cu anticathode. The instrument was operated in the following conditions: accelerating voltage of 40 kV and a current intensity of 40 mA; the wide-angle goniometer radius is 185 mm. The scanning parameters were: 2θ ranges from 5 to 158°; typical 2θ step size of

Table 4. WDS calibration standards, crystal monochromators, and detection limits for sulphides

Chemical element (Symbol)	Standard mineral name	Monochomator crystal acronym	Standard deviation (SD/%)	Detection limit (w_{DL}/ppm wt.)
Antimony (Sb)	Stibnite	PETJ	0.36	434
Arsenic (As)	Arsenopyrite	TAP	0.61	633
Copper (Cu)	Chalcopyrite	LiF	0.46	413
Cobalt (Co)	CoNiAs	LiF	0.29	326
Iron (Fe)	Pyrite	LiFH	0.23	235
Sulphur (S)	Pyrite	PETJ	0.30	170

Notes: 1) LiF = Lithium fluoride; LiFH = Lithium fluoride; TAP = Thallium acid phtalate; PETJ = Pentaerythritol with Johansson geometry and 2) standard deviation is given for a confidence interval of 95% (i.e., 2σ).

Table 5. EPMA chemical analysis and atomic fractions of major titanates phases

Mineral Phase	Ilmenite (BO)	Hematite (BO)	Ilmenite (RO)	Hematite (RO)	Magnetite (RO)	Ilmenite (URO)	Magnetite (URO)
No. analysis	4	4	3	6	3	3	6
Oxides	Oxides mass fraction (%wt.)						
TiO_2	48.5488	11.3968	44.2503	14.2245	0.7026	45.5057	11.7136
MgO	3.1175	0.4724	3.2240	1.2655	0.1852	3.0935	0.9342
FeO/Fe_2O_3	46.7865	**86.6873**	48.3033	**83.2937**	97.5069	48.8735	**86.2406**
Al_2O_3	0.0000	0.1810	0.0000	0.2316	0.2249	0.0430	0.1640
CaO	0.0000	0.0000	0.0000	0.0000	0.0000	0.0000	0.0000
MnO/Mn_2O_3	0.1900	0.0000	0.1903	**0.0853**	0.0000	0.1928	0.0520
V_2O_3/V_2O_5	0.1058	**0.6147**	0.1153	**0.4813**	**0.2675**	0.1568	**0.5764**
Cr_2O_3	0.0000	0.3712	0.0840	0.3899	0.9512	0.0000	0.3112
SiO_2	0.0000	0.0000	0.0000	0.0000	0.0000	0.0000	0.0000
NiO	0.0000	0.0000	0.0000	0.0000	0.1615	0.0000	0.0000
CoO	0.0000	0.0000	0.0000	0.0000	0.0000	0.0000	0.0000
Total (wt.%) =	98.7485	99.7233	96.1673	99.9718	99.9997	97.8653	99.9920

Atoms	Atom per formula unit (apfu) based on the number of oxygen anions listed at the bottom of each columns						
Ti	0.9356	0.2195	0.8902	0.2702	0.0202	0.8979	0.3206
Mg	0.1191	0.0180	0.1285	0.0476	0.0106	0.1210	0.0507
Fe	1.0023	1.6698	1.0803	1.5824	2.9050	1.0720	2.4429
Al	0.0000	0.0055	0.0000	0.0069	0.0101	0.0013	0.0070
Ca	0.0000	0.0000	0.0000	0.0000	0.0000	0.0000	0.0000
Mn	0.0041	0.0000	0.0043	0.0018	0.0000	0.0043	0.0016
V	0.0022	0.0126	0.0025	0.0097	0.0082	0.0033	0.0168
Cr	0.0000	0.0075	0.0018	0.0078	0.0288	0.0000	0.0090
Si	0.0000	0.0000	0.0000	0.0000	0.0000	0.0000	0.0000
Ni	0.0000	0.0000	0.0000	0.0000	0.0050	0.0000	0.0000
Co	0.0000	0.0000	0.0000	0.0000	0.0000	0.0000	0.0000
O	3	3	3	3	4	3	4
Total (at.) =	5.063	4.933	5.108	4.926	6.988	5.100	6.849

Titanate (SOREL)	Pseudorutile (ORPO)	Rutile (ORPO)	Rutile (HTS)	Neo-ilmenite (HTS)	Rutile core (UGS)	Rutile rim (UGS)	Pseudorutile (UGS)
6	8	3	3		3	3	1
84.6535	83.8493	99.1453	98.9656	53.4823	88.5436	98.9656	77.9454
5.2935	5.5243	0.0000	0.0000	3.8207	4.4415	0.0000	7.0262
6.8543	7.5467	0.3979	0.3241	38.8000	4.4307	0.3241	11.2961
2.0253	1.9976	0.0576	0.0000	0.2767	1.4924	0.0000	2.2564
0.0000	0.0000	0.0000	0.0000	0.0000	0.0379	0.0000	0.0000
0.1328	0.2070	0.0925	0.0000	0.3740	0.1594	0.0000	0.4749
0.5443	0.6305	0.2141	0.5467	0.2450	0.6874	0.5467	0.5983
0.1815	0.2078	0.0000	0.0851	0.1617	0.1549	0.0851	0.3505
0.0000	0.0000	0.0000	0.0000	0.0000	0.0000	0.0000	0.0000
0.0000	0.0000	0.0000	0.0000	0.0000	0.0000	0.0000	0.0000
0.0000	0.0000	0.0000	0.0000	0.0000	0.0000	0.0000	0.0000
99.6853	99.9630	99.9074	99.9216	97.1603	99.9478	99.9216	99.9478
2.1876	3.9060	0.9933	0.9917	1.0067	0.8940	0.9909	3.6977
0.2711	0.5099	0.0000	0.0000	0.1425	0.0889	0.0000	0.6604
0.1969	0.3908	0.0040	0.0012	0.8118	0.0447	0.0032	0.5957
0.0820	0.1457	0.0009	0.0009	0.0082	0.0236	0.0000	0.1677
0.0000	0.0000	0.0000	0.0000	0.0000	0.0005	0.0000	0.0000
0.0039	0.0109	0.0009	0.0000	0.0079	0.0016	0.0000	0.0254
0.0150	0.0258	0.0019	0.0046	0.0049	0.0061	0.0048	0.0249
0.0049	0.0102	0.0000	0.0013	0.0032	0.0016	0.0009	0.0175
0.0000	0.0000	0.0000	0.0000	0.0000	0.0000	0.0000	0.0000
0.0000	0.0000	0.0000	0.0000	0.0000	0.0000	0.0000	0.0000
0.0000	0.0000	0.0000	0.0000	0.0000	0.0000	0.0000	0.0000
5	9	2	2	3	2	2	9
7.761	13.999	3.001	3.000	4.985	3.061	3.000	14.189

Table 6. EPMA chemical analysis and atomic fractions of major sulphide and sulfosalts phases

Mineral phase	Pyrite (BO)	Millerite (BO)	Chalcopyrite (BO)	Pyrrhotite (BO)	Troilite (RO)
No. analysis	3	1	3	3	1
Elements	Element mass fraction (wt.%)				
Fe	45.3000	1.1600	30.3700	52.5033	63.0867
Cu	0.0000	0.0000	34.4600	1.9467	0.1600
Ni	0.0907	64.0800	0.0000	6.1500	0.0000
Co	1.3143	0.1130	0.0000	1.1200	0.0000
As	0.0000	0.0000	0.0053	0.0190	0.0137
Sb	0.0000	0.0000	0.0000	0.0000	0.0000
S	53.3567	35.2700	34.9167	37.5733	35.9600
Total (wt.%) =					
	Atom per formula unit (apfu) based on the number of sulphur atoms listed at the bottom of each columns				
Fe	0.9750	0.0189	0.9989	0.8024	1.0073
Cu	0.0000	0.0000	0.9960	0.0261	0.0022
Ni	0.0019	0.9926	0.0000	0.0894	0.0000
Co	0.0268	0.0017	0.0000	0.0162	0.0000
As	0.0000	0.0000	0.0001	0.0002	0.0002
Sb	0.0000	0.0000	0.0000	0.0000	0.0000
S	2.0000	1.0000	2.0000	1.0000	1.0000
Total (at.) =	3.004	2.013	3.995	1.934	2.010

Table 7. EPMA chemical analysis and atomic fractions of major silicates

Mineral phase	Andesine (BO)	Orthose (BO)	Chlorite (BO)	Enstatite (RO)	Phlogopite (BO)	Andesine (RO)	Phlogopite (RO)	Andesine (URO)	Titanite (SOREL)
No. analysis	2	1	4	2	6	1	1	3	1
Oxides	Oxides mass fraction (%wt.)								
TiO$_2$	0.0000	0.0000	0.1087	0.2325	5.3340	0.0000	5.2800	0.0000	39.5750
MgO	0.0000	0.0000	22.7287	24.8925	18.1220	0.0000	18.6090	0.0000	0.0000
FeO	0.1140	0.0830	16.9987	20.0455	9.4360	0.0950	7.9770	0.2997	0.4290
Al$_2$O$_3$	26.9995	18.3810	16.4147	2.0595	15.7100	26.6730	16.1780	27.2640	0.9580
CaO	9.1660	0.0440	0.2423	0.5695	0.0000	9.3430	0.0000	10.5273	28.8880
MnO	0.0000	0.0000	0.0000	0.3035	0.0000	0.0000	0.0000	0.0000	0.0000
Na$_2$O	6.0895	0.4700	0.0000	0.0000	0.0000	5.9020	0.2370	5.3043	0.0000
Cr$_2$O$_3$	0.0000	0.0000	0.0000	0.0000	0.0000	0.0000	0.0000	0.0000	0.0000
SiO$_2$	57.2755	64.3380	32.2700	52.3785	37.4040	57.2530	37.3660	52.2877	30.6000
K$_2$O	0.2795	16.7900	0.0000	0.0000	10.5980	0.5780	10.4220	0.2693	0.0000
H$_2$O			11.0840		3.3170		3.8310		
Total (wt %) =	99.9240	100.106	99.8470	100.4815	99.9210	99.8440	99.9000	95.9523	100.4500

(*Continued*)

13

Table 7. Continued

Mineral phase	Andesine (BO)	Orthose (BO)	Chlorite (BO)	Enstatite (RO)	Phlogopite (BO)	Andesine (RO)	Phlogopite (RO)	Andesine (URO)	Titanite (SOREL)
No. analysis	2	1	4	2	6	1	1	3	1
Atoms	Atom per formula unit (apfu) based on the number of oxygen anions listed at the bottom of each columns								
Ti	0.0000	0.0000	0.0082	0.0064	0.2948	0.0000	0.2883	0.0000	0.9682
Mg	0.0000	0.0000	3.4063	1.3619	1.9848	0.0000	2.0134	0.0000	0.0000
Fe	0.0043	0.0032	1.4292	0.6152	0.5798	0.0036	0.4842	0.0118	0.0117
Al	1.4279	1.0049	1.9449	0.0891	1.3603	1.4141	1.3838	1.5155	0.0367
Ca	0.4407	0.0022	0.0261	0.0224	0.0000	0.4503	0.0000	0.5320	1.0066
Mn	0.0000	0.0000	0.0000	0.0094	0.0000	0.0000	0.0000	0.0000	0.0000
Na	0.5298	0.0423	0.0000	0.0000	0.0000	0.5148	0.0333	0.4851	0.0000
Cr	0.0000	0.0000	0.0000	0.0000	0.0000	0.0000	0.0000	0.0000	0.0000
Si	2.5701	2.9846	3.2442	1.9223	2.7480	2.5755	2.7119	2.4661	0.9951
K	0.0160	0.9936	0.0000	0.0000	0.9933	0.0332	0.9649	0.0162	0.0000
H			7.4327		1.6255		1.8546		
O	8	8	18	6	12	8	12	8	5
Total (at.) =	12.989	13.031	35.492	10.027	21.586	12.991	21.734	13.027	8.018

14

$0.02°$; measuring time from 1 to 5 s per step. The phase identification was performed using the software JADE version 3.1 (Materials Data, Inc., Livermore, California, USA) (1997).

Chemical Quantitative Analysis

The general procedure utilized for conducting the quantitative chemical analysis of titania-rich products is depicted schematically in Figure 3.

Literature data regarding the chemistry and mineralogy of titanates being relatively scarce a classification of titanates according to both
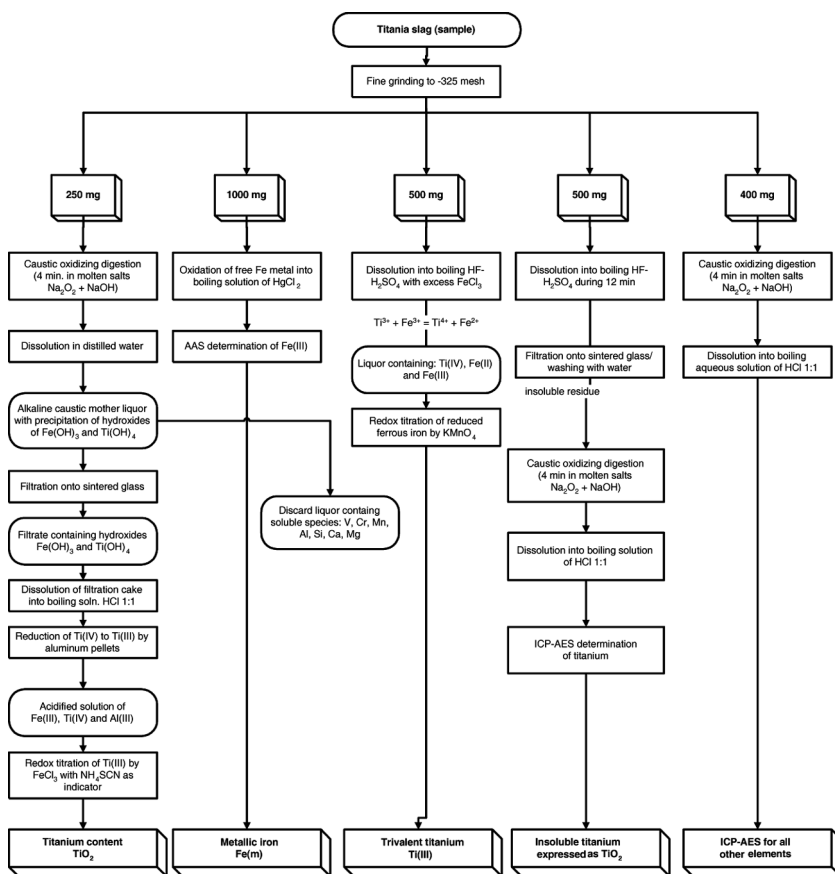
Figure 3. General procedure for quantitative chemical analysis of titania-rich products at QIT.

crystal structure and chemistry is presented in the appendices in Table 12, while the major properties and characteristics of natural and synthetic titanate minerals occurring in titania-rich slags and related products are summarized in Table 13. Moreover, in order to identify the various phases and minerals discussed in this article, without confusion the *Chemical Abstract Registry Number* (CARN) of each natural or synthetic mineral phase is also provided and written in square brackets after each mineral name the first time it appears in the text.

RESULTS AND DISCUSSION

Ore Beneficiation

The chemistry and mineralogy of the titania-rich slag and its iron coproduct is obviously related to the chemical and mineralogical composition of the hemo-ilmenite concentrate, and, in a lesser extent, to that of the anthracite coal. Therefore, a brief description of the ore is given hereafter. After common ore beneficiation techniques (Guimond 1964) (e.g., comminution, sizing, and gravity separation), the *run-of-mine* (ROM) yields a *beneficiated ore* (BO) with 34.5 mass percent TiO_2 (Table 8). A flow sheet of the entire beneficiation process is presented in Figure 4. Microscopic examination reveals an intimate exsolution texture intergrowth of hematite [1309-37-1] Fe_2O_3, lamellae into ilmenite [12168–52-4] $FeTiO_3$ grains and conversely exsolution lamellae of ilmenite into hematite grains (Figure 5). This kind of fractal microstructure (Mandelbrot 1986) indicates a progressive cooling of the parent magma from which originated the ore body. The average mass fractions of ilmenite and hematite in the grains are 70 and 30 wt.%, respectively (i.e., 69 mol.% and 31 mol.%). For that reason, the ore is usually called hemo-ilmenite. Other ubiquitous gangue minerals coming from the anorthosite host rock, such as silicates, oxides, sulphides, and sulfosalts, are also present along with hemo-ilmenite grains.

The detailed mineralogical composition of the ROM performed in the 1970s (Bergeron 1986). In situ electron probe microchemical analysis (EPMA) gives the following averaged chemical formula for the Allard Lake ilmenite $(Fe_{1.002}Mg_{0.119}Mn_{0.004}V_{0.002})Ti_{0.936}O_3$. As expected from crystallochemical considerations, the crystal lattice of the ilmenite hosts divalent metal cations having ionic radii close to that of Fe^{2+} (61 pm), such as Mg^{2+} (72 pm) and Mn^{2+} (83 pm). These cations substitute

Table 8. Typical chemical composition of titania-rich products from QIT (mass %)

Titania-rich product (QIT acronym)	TiO$_2$ (tot)	TiO$_2$	Ti$_2$O$_3$*	Fe^0	FeO	Fe$_2$O$_3$	MgO	SiO$_2$	Al$_2$O$_3$	V$_2$O$_5$	CaO	MnO	Cr$_2$O$_3$	S
Run-of-mine (ROM)	32.7	32.7	nil	nil		37.0**	2.92	6.65	4.14	0.30	1.10	0.12	0.13	0.32
Beneficiated ore (BO)	34.5	34.5	nil	nil		38.2**	2.77	4.93	3.28	0.31	0.77	0.13	0.13	0.22
Roasted ore (RO)	34.8	34.8	nil	nil		38.9**	2.69	4.55	3.13	0.33	0.76	0.12	0.13	0.04
Upgraded roasted ore (URO)	37.60	37.60	nil	nil	29.90	27.20	2.70	0.8	0.8	0.3	0.2	0.1	0.10	
Sorelslag	80.00	62.00	18.00	0.50	9.70	nil	5.30	2.60	2.40	0.60	0.50	0.30	0.20	0.084
Oxidized slag (ORPO)	81.84					7.66	5.02	1.50	2.31	0.61	0.35	0.22	0.16	0.009
Heat treated titania slag (HTS)	80.54	72.14	8.40			9.66	5.17	1.59	2.37	0.62	0.29	0.23	0.19	0.004
Upgraded titania slag (UGS)	94.50	94.50	nil	nil	nil	1.5	0.7	1.80	0.50	0.40	0.1	0.01	0.10	0.008

(*) Ti$_2$O$_3$ expressed as TiO$_2$; (**) expressed as Fe(total).
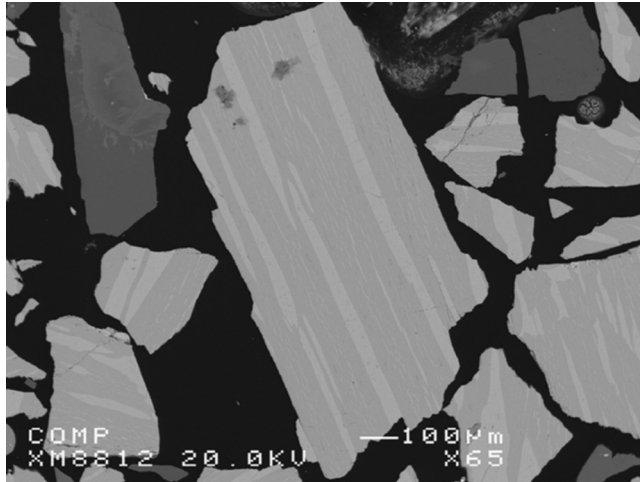
Figure 4. Hemo-ilmenite ore beneficiation process.
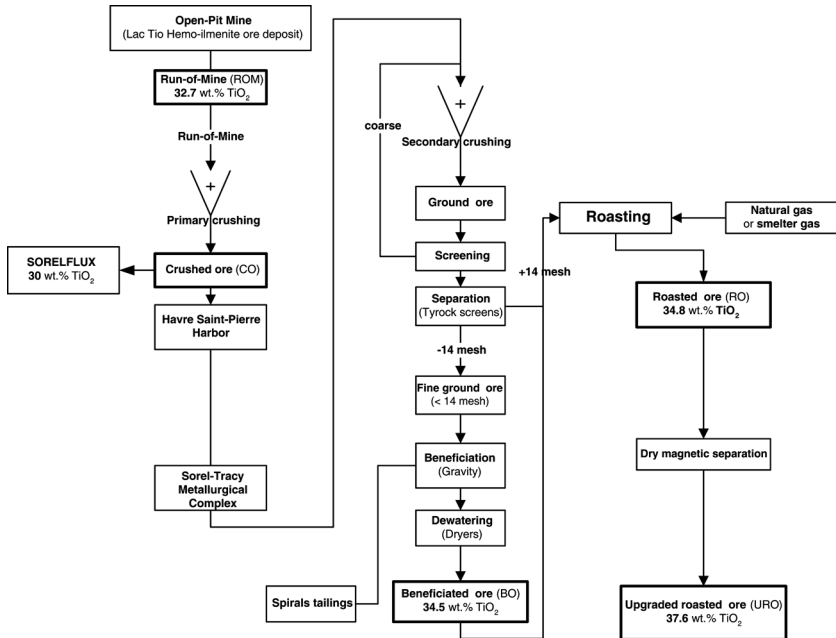
Figure 5. Beneficiated ore (BO) (hemo-ilmenite crystal showing hematite exsollution lamellae).

isomorphically to the iron and occupy the octahedral sites forming a solid solution in the ilmenite–giekielite–pyrophanite series ($MTiO_3$, with $M = Fe^{2+}$, Mg^{2+}, and Mn^{2+}) (Donald 1976). This behavior is also observed for other hard-rock hemo-ilmenites worldwide (Robinson et al. 2001). On the other hand, the microchemical analysis revealed that the hematite lamellae exhibit the following average chemical formula $(Fe_{0.835}Ti_{0.110}Mg_{0.009}V_{0.007}Cr_{0.004}Al_{0.003})_2O_3$, showing that minor trivalent metal cations, especially V^{3+} (64 pm), Al^{3+} (54 pm), and Cr^{3+} (62 pm) with a ionic radius close to that of Fe^{3+} (55 pm), substitute isomorphically to iron in the crystal lattice of hematite forming a solid solution in the hematite–karelianite–corundum–eskolaite series (M_2O_3 with $M = Fe^{3+}$, Al^{3+}, Cr^{3+}, V^{3+}, Ti^{3+}). The presence of some magnesium and titanium is due to the fact that it is not possible with the electron microprobe beam to isolate and analyze a region free of tiny exsolution lamellae of ilmenite that are always present and with a size well below the resolution of the equipment.

The major part of the silica, alumina, and calcia present in the ore comes from gangue minerals such as the plaglioclase feldspar andesine [1302–54-1] with an average mineralogical composition that can be expressed as a combination of anorthite ($An = CaAl_2Si_2O_8$), albite ($Ab = NaAlSi_3O_8$), and orthoclase ($Or = KAlSi_3O_8$) as $An_{47}Ab_{47}Or_6$. The other important silicate minerals are mica phlogopite [12251-58-0] $KMg_3(Si_3Al)O_{10}(F,OH)_2$, with the average empirical formula $K_{0.993}$ $(Mg_{1.985}Fe_{0.580})Si_{2.742}Al_{1.360}O_{10}(OH_{0.813})_2$, chlorite with the empirical formula $(Mg_{3.406}Fe_{1.429}Al_{0.945})Si_{3.244}AlO_{10}(OH_{0.929})_8$, enstatite $(Fe,Mg)_2Si_2O_6$ with the empirical formula $Fe_{0.615}Mg_{1.362}Si_{1.922}O_6$, and to a lesser extent titanite $CaTiOSiO_4$ with the empirical formula $Ca_{1.007}Ti_{0.968}Si_{0.995}O_5$. The major oxide minerals is the ferroan spinel [1302-67-6] $(Mg_{0.72}Fe_{0.28})(Al_{0.96}Fe_{0.04})_2O_4$. Finally, trace elements such as nickel and cobalt come mainly from Ni- and Co-rich sulphides and sulfosalts minerals such as millerite [16812-54-7] NiS with empirical formula $Ni_{0.993}Fe_{0.019}Co_{0.002}S$, siegenite [12174-56-0] $(Ni,Co)_3S_4$, cobaltite [1303–15-7] $(Co,Fe)AsS$, and linnaeite [1308-08-3] Co_3S_4 and to a lesser extent pyrite [1317-66-4] FeS_2, $Fe_{0.975}Co_{0.027}Ni_{0.002}S_2$ and pyrrhotite [1310-50-5] $Fe_{1-x}S$, with an average formula $Fe_{0.802}Ni_{0.089}Cu_{0.026}Co_{0.016}S_2$ while most of the copper comes from chalcopyrite [1308-56-1] $(CuFeS_2)$ $Cu_{0.999}Fe_{0.996}S_2$. Because, the mixture of ilmenite and hematite is so fine grained, an intricate comminution techniques cannot liberate the two phases. The beneficiated ore is then subjected to an oxidative roasting

Table 9. Typical chemical composition of iron products from QIT (mass %$_{max}$)

Iron product	Fe	C	Mn	S	P	Si	Cu	Ni	Cr	Sn	Mo	Al	V	N	Co
Sorelmetal[®]*	bal.	4.7	0.015	0.015	0.030	0.40	0.03	0.08	0.05	0.0011	0.005	0.005	0.040	—	0.025
Sorelsteel[®]	bal.	0.73	0.55	0.015	0.020	0.25	0.08	0.08	0.07	0.005	0.005	0.005	0.008	0.06	0.05

*As tapped.

Table 10. Oxidation mechanisms occuring during the roasting of ilmenite adapted from Haggerty (1976)

Mechanism	Description	Solid state reactions	Magnetic behavior of products
No. 1	Homogenous unoxidized Ilmenite	$FeTiO_3$ and Fe_2O_3 in exsollution lamellae	Antiferromagnetic ilmenite
No. 2	First signs of oxidation with the formation of fine rutile lenses and ferrian ilmenite.	$9FeTiO_3 \cdot Fe_2O_3 + O_2$ $\rightarrow 5FeTiO_3 \cdot 3Fe_2O_3 + 4TiO_2$	Antiferromagnetic ilmenite
No. 3	Diffusion continues, the lenses thicken, Ti diffuses from the ferrian ilmenite to the rutile. Rim of whiter ferrian ilmenite form around the rutile grains.	$9FeTiO_3 \cdot Fe_2O_3 + O_2$ $\rightarrow 5FeTiO_3 \cdot 3Fe_2O_3 + 4TiO_2$	Antiferromagnetic ferrian ilmenite
No. 4	Oxidation, the two mineral phases present in step 1 & 2	$9FeTiO_3 \cdot Fe_2O_3 + 2O_2 \rightarrow 0.9FeTiO_3 \cdot Fe_2O_3$ $+ 0.1FeTiO_3 \cdot 4Fe_2O_3 + 8TiO_2$ $5FeTiO_3 \cdot 3Fe_2O_3 + 4TiO_2$ $\rightarrow 0.1FeTiO_3 \cdot 0.4Fe_2O_3 + 8TiO_2$ $5FeTiO_3 \cdot 3Fe_2O_3 + 4TiO_2 \rightarrow 3FeTiO_3 \cdot 3Fe_2O_3$ $+ 2FeTiO_3 \cdot 2Fe_2O_3 + 4TiO_2$	Ferrimagnetic ferrian ilmenite Antiferromagnetic titanohematite Antiferromagnetic titanohematite Antiferromagnetic ferrian ilmenite
No. 5	Continuation of steps 2 and 3 by means of diffusion	$9FeTiO_3 \cdot Fe_2O_3 + 2O_2 \rightarrow 0.9FeTiO_3 \cdot Fe_2O_3$ $+ 0.1FeTiO_3 \cdot 0.4Fe_2O_3 + 8TiO_2$	Ferrimagnetic ferrian ilmenite

(*Continued*)

Table 10. Continued

Mechanism	Description	Solid state reactions	Magnetic behavior of products
No. 6	This mechanism occurs when pseudobrookite starts to appear through the oxidation of original ilmenite, and through the oxidation of the previous oxidation/diffusion products.	$9FeTiO_3 \cdot Fe_2O_3 + O_2 \rightarrow 4FeTiO_3 \cdot Fe_2O_3$ $+ 2Fe_2TiO_5 \cdot FeTi_2O_5 + TiO_2$	Antiferromagnetic ferrian ilmenite Ferropseudobrookite ferrian
		$9FeTiO_3 \cdot Fe_2O_3 + 0.5O_2 \rightarrow FeTiO_3 \cdot Fe_2O_3$ $+ 3Fe_2TiO_5 \cdot 2FeTi_2O_5 + TiO_2$	Ferrimagnetic ferrian ilmenite Ferrospseudobrookite
		$5FeTiO_3 \cdot 3Fe_2O_3 + 4TiO_2 + 0.5O_2$ $\rightarrow 2FeTiO_3 \cdot Fe_2O_3 + 3Fe_2TiO_5 \cdot 2FeTi_2O_5 + 2TiO_2$	Ferrimagnetic ferrian ilmenite Ferrospseudobrookite
		$3FeTiO_3 \cdot Fe_2O_3 + 2FeTiO_3 \cdot 2Fe_2O_3$ $+ 4TiO_2 + 0.5O_2 \rightarrow 2FeTiO_3 \cdot 2Fe_2O_3$ $+ 2Fe_2TiO_5 \cdot FeTi_2O_5 + 3TiO_2$	Ferrimagnetic ferrian ilmenite Ferrospseudobrookite
No. 7	Direct ilmenite to pseudobrookite at >800°C	$9FeTiO_3 \cdot Fe_2O_3 + 2O_2$ $\rightarrow 5Fe_2TiO_5 \cdot FeTi_2O_5 + 2TiO_2$	Ferropseudobrookite
		$9FeTiO_3 \cdot Fe_2O_3 + 1.5O_2$ $\rightarrow 3Fe_2TiO_5 \cdot 3FeTi_2O_5 + Fe_2O_3$	Pseudobrookite–ferropseudobrookite Hematite
		$5FeTiO_3 \cdot 3Fe_2O_3 + 4TiO_2 + O_2$ $\rightarrow 5Fe_2TiO_5 \cdot 3FeTi_2O_5 + 2TiO_2$	Ferropseudobrookite
		$5FeTiO_3 \cdot 3Fe_2O_3 + 4TiO_2 + 0.5O_2$ $\rightarrow 3Fe_2TiO_5 \cdot 3FeTi_2O_5 + Fe_2O_3$	Pseudobrookite–ferropseudobrookite Hematite

to allow: 1) the oxidation of sulphide and sulfosalt minerals for the removal of most of the sulphur content and 2) the formation of ferromagnetic domains within the hemo-ilmenite grains, to allow their magnetization in order to render easier their separation from residual gangue minerals (Cui et al. 2002). Actually, hematite and ilmenite are antiferromagnetic minerals and the roasting step induces atomic reordering within the ilmenite and hematite crystal lattices that modify their magnetic behavior. For instance, there is a region in the ternary phase diagram FeO-Fe_2O_3-TiO_2 where the ilmenite-hematite becomes ferrimagnetic. In the solid solution range, compositions comprised from pure hematite up to $Ilm_{0.5}Hem_{0.5}$ act like antiferromagnetic hematite, while domains ranging between $Ilm_{0.5}$-$Hem_{0.5}$ to $Ilm_{0.75}Hem_{0.25}$ yield to grains that act ferrimagnetically. Grains with a composition ranging between $Ilm_{0.85}Hem_{0.15}$ and pure ilmenite are all antiferromagnetic, while samples with empirical formula between $Ilm_{0.75}Hem_{0.25}$ and $Ilm_{0.85}Hem_{0.15}$ exhibit a hysteresis memory and strong remnant magnetization.

Therefore, an efficient roasting step must produce a ferrian ilmenite with a composition ranging between $Ilm_{0.50}Hem_{0.50}$ to $Ilm_{0.75}Hem_{0.25}$. Compositions between $Ilm_{0.75}Hem_{0.25}$ to $Ilm_{0.85}Hem_{0.15}$ are not detrimental to magnetic separation, but anything with a composition between pure hematite and $Ilm_{0.5}Hem_{0.5}$ and between pure ilmenite and $Ilm_{0.85}Hem_{0.15}$ is detrimental. During roasting, the original ilmenite particle does not change; rather, the distribution of iron and titanium within domains of the particle is altered through oxidation and diffusion, therefore altering the mineralogy. The mechanism of oxidation of ilmenite can be divided into seven stages (Haggerty 1976). These stages are interpreted from the oxidation of ilmenite observed inside igneous rocks, but the chemical reactions involved can also be extended to synthetic processes as well and are presented for information in Table 10. In our case, only Step 7 in Haggerty's classification is relevant to understand the final products obtained during the roasting of the QIT's hemo-ilmenite.

During roasting conducted in air, the ore is treated at a temperature ranging between 900°C and 1000°C. The hematite of the grain reacts with part of FeO from the ilmenite to produce magnetite [1317-61-9] Fe_3O_4 and pseudobrookite [1310-39-0] Fe_2TiO_5 (Briggs and Sacco 1993) (Figure 6) according to the theoretical chemical reaction

$$FeTiO_3 + 2Fe_2O_3 \rightarrow Fe_3O_4 + Fe_2TiO_5.$$
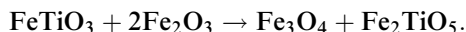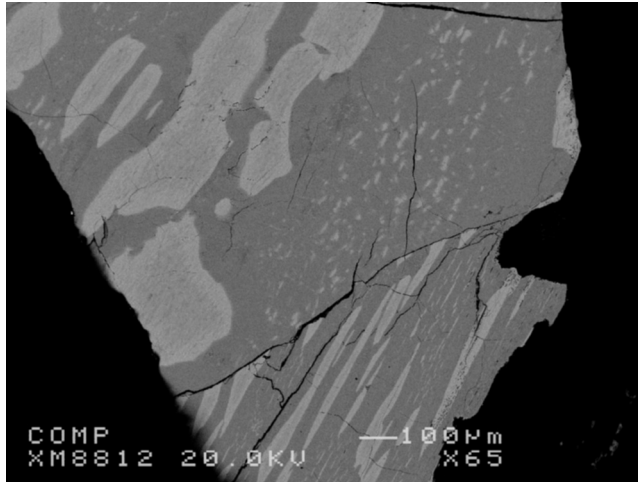
Figure 6. Roasted ore (RO) (hemo-ilmenite grain showing magnetite and pseudobrookite around former hematite grains).

In practice, the actual composition of the hemo-ilmenite must be considered in the roasting equation and the actual reaction can be described according to the following reaction scheme, which also tracks the behavior of minor and traces elements based on the microprobe analysis of each phase identified:

$$0.69(Fe, Mg, Mn)TiO_3 + 0.31(Fe, V, Al, Cr)_2O_3 + (Co, Ni)_xO_y$$
$$\rightarrow 0.53(Fe, Mg, Mn)TiO_3 + 0.16(Fe, Mg)_2TiO_5$$
$$+ 0.16(Fe, Mg, Ni)(Fe, V, Al, Cr, Mn, Co)_2O_4.$$
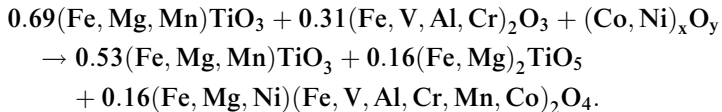
From the above reaction scheme, it can be seen that at the end of the roasting process, the excess ilmenite is the major mineral phase along with hematite, magnetite, and pseudobrookite. The averaged empirical formula of the excess ilmenite determined by EPMA is $(Fe_{1.080}Mg_{0.129}Mn_{0.004}Cr_{0.002}V_{0.002})Ti_{0.890}O_3$, which is close to that of the original ilmenite in the beneficiated ore. As expected, the ilmenite grains still host most of the manganese and magnesium while traces of vanadium and chromium comes mainly from tiny inclusions of hematite.

The magnetite appears at the boundaries of ilmenite-hematite forming large rims around ilmenite with the empirical formula $(Fe_{0.968}Cr_{0.010}Ti_{0.007}Mg_{0.004}V_{0.003}Al_{0.003}Ni_{0.002})_3O_4$ while the remaining

hematite grains exhibits the formula $(Fe_{0.791}Ti_{0.135}Mg_{0.024}V_{0.005}$-$Cr_{0.004}Al_{0.0035}Mn_{0.001})_2O_3$. Some tests were also performed at the laboratory scale at Rio Tinfo Iron & Titanium (RIT) to better understand the above solid-state reactions occurring during the roasting process. A sample of hemo-ilmenite ore was heated in air inside a box furnace at 1100°C for 1 h. From Figure 7 we can observe the thick layer of pseudobrookite surrounding the hematite lamellae.

From these empirical formulae we can clearly see the pathways followed by minor elements during solid-state reactions. For minor elements originally in solid solution into the hematite lattice such as Al^{3+}, V^{3+}, and Cr^{3+} along with some magnesium and titanium coming from the ilmenite grains, they follow the Fe^{3+} into the magnetite grains. Actually, the spinel structure accommodates a wide variety of mixed valence metal cations (AB_2O_4 with A = Fe^{2+}, Mg^{2+}, Ni^{2+}, and B = Fe^{3+}, Cr^{3+}, Al^{3+}, V^{3+}, Mn^{3+}, and Co^{3+}). Therefore, the neoformed magnetite mineral in the roasted treated ore can be seen as a solid solution between pure magnetite and minerals having the spinel structure, such as magnesioferrite [12023-16-4] $MgFe_2O_4$, ulvospinel [12063-18-2] $FeTi_2O_4$, and to a lesser extend chromite [1308-31-2] $FeCr_2O_4$, hercynite [1302-61-0] $FeAl_2O_4$, coulsonite [12418-94-9] FeV_2O_4, manganese ferrite [12063-10-4] $MnFe_2O_4$, trevorite [12186-55-9] $NiFe_2O_4$, and cobalt ferrite [12052-28-7] $CoFe_2O_4$.
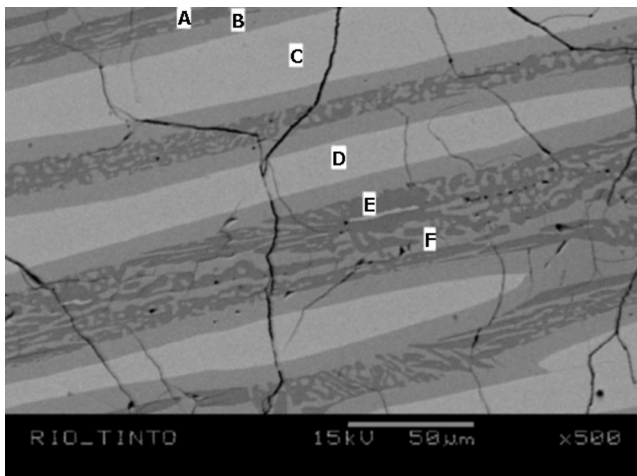
Figure 7. Hemo-ilmenite ore heated in air at 1100°C (1 h) (C, D = hematite; B = pseudobrookite; and A, E, and F = ilmenite).
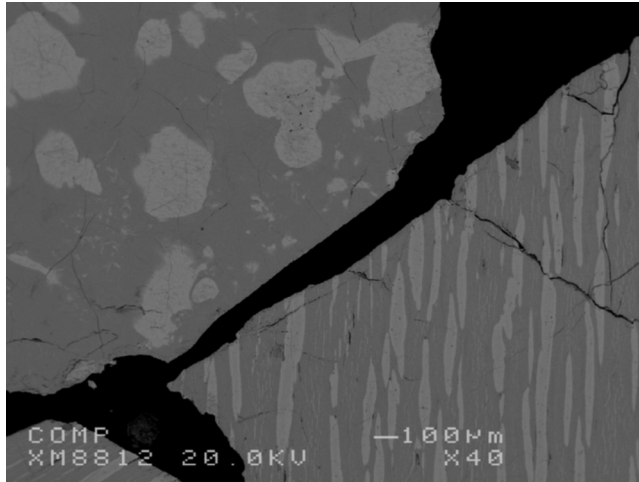
Figure 8. Upgraded roasted ore (URO) (roasted hemo-ilmenite grain along with unreacted hemo-ilmenite).

Moreover, all sulphides and sulfosalts are oxidized during roasting giving-off sulphur dioxide (SO_2), which is later absorbed into the off-gases scrubbers while most of the cobalt and nickel accommodate the spinel structure of the magnetite, as mentioned previously. During roasting, most of the plagioclase feldspar along with phlogopite mica and spinel remain unaffected, as indicated by their empirical formulae $Na_{0.515}Ca_{0.450}K_{0.480}$-$Si_{2.575}Al_{1.414}O_8$ and $K_{0.965}(Mg_{2.013}Fe_{0.484})Si_{2.712}Al_{1.384}O_{10}(OH_{0.927})_2$.

After roasting, the *roasted ore* (RO) is subjected to a magnetic separation (Bergeron and Priest 1976)using rare earths magnets that remove most ore from the nonmagnetic gangue materials, especially plagioclases, spinel, and phlogopite mica that form the black tailings. The resulting *upgraded roasted ore* (URO) Figure 8 is then transported into the electric arc furnace. The mineralogy of the titanates phases existing in the upgraded roasted treated ore are obviously the same as those existing in the roasted ore as confirmed by the empirical formulae of ilmenite $(Fe_{1.072}Mg_{0.121}Mn_{0.004}V_{0.003}Al_{0.001})Ti_{0.898}O_3$, of magnetite $(Fe_{0.968}Cr_{0.010}Ti_{0.007}Mg_{0.004}V_{0.003}Al_{0.003}Ni_{0.002})_3O_4$ and hematite grains $(Fe_{0.8143}Ti_{0.107}Mg_{0.017}V_{0.006}Cr_{0.003}Al_{0.002}Mn_{0.001})_2O_3$, except the fact that most of the gangue minerals are now removed.

Electric Arc Smelting—During the electrothermal reduction of the upgraded roasted ore with anthracite coal as carbonaceous reductant

into an EAF using a transferred arc, the reduction takes place rapidly (Figure 9). The strong reducing conditions ensure that iron oxides values are almost completely reduced to metallic iron while titanium dioxide TiO_2 is partially reduced to titanium sesquioxide Ti_2O_3. All these reactions evolve carbon monoxide (CO) according to the following reaction schemes with their Gibbs molar enthalpies calculated at 2000 K (Chase 1998) and expressed per mole of oxide:

$$Fe_2O_3(s) + C(s) \rightarrow 2FeO(l) + CO(g) \quad \Delta_R G_{2000}^0 K = -269.528\,kJ.mol^{-1}$$

$$FeO(s) + C(s) \rightarrow Fe(l) + CO(g) \quad \Delta_R G_{2000}^0 K = -137.582\,kJ.mol^{-1}$$

$$2TiO_2(s) + C(s) \rightarrow Ti_2O_3(s) + CO(g) \quad \Delta_R G_{2000}^0 K = -51.204\,kJ.mol^{-1}$$
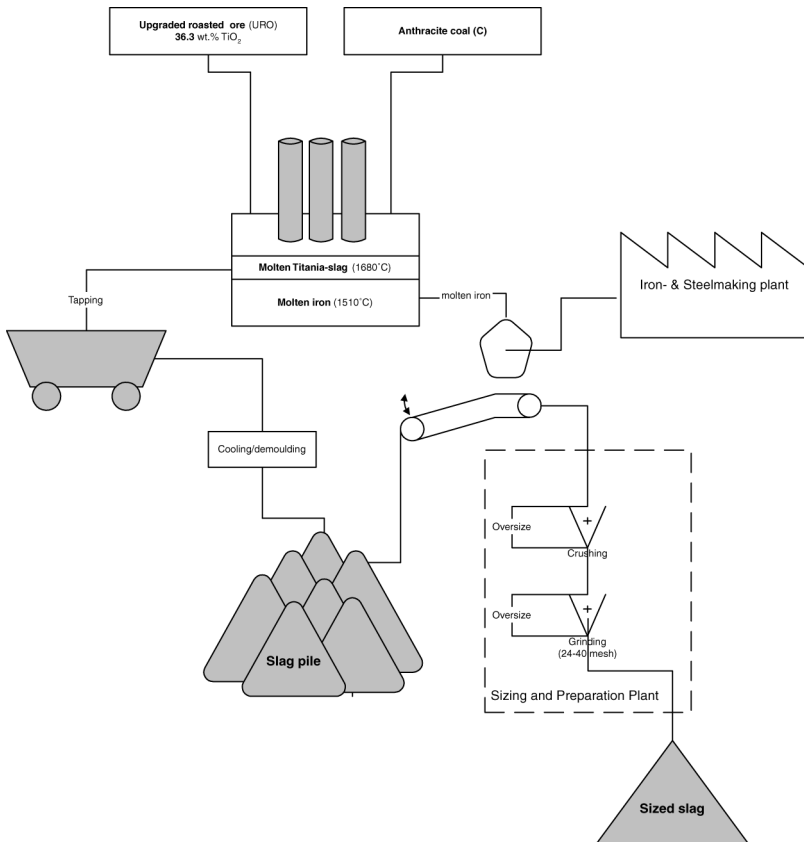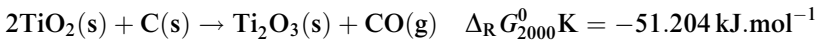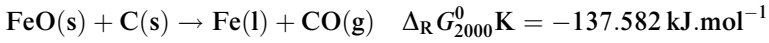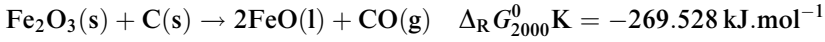
Figure 9. Titania slag EAF smelting process.

If we consider the initial chemical composition of the hemo-ilmenite ore, the chemical composition of the Sorelslag as tapped, and the sensible and latent heats required to bring the feed materials at the operating temperature, the theoretical specific energy consumption of the smelting process is about 0.903 kWh per kilogram of ore. Due to the inescapable trace of moisture and the volatile matter (VM) of the anthracite coal, some hydrogen forms and combines to the carbon monoxide to yield the smelter gas (i.e., $CO + H_2$). At the high temperature existing in the furnace, iron forms dense liquid droplets ($\rho = 6800 \, \text{kg} \cdot \text{m}^{-3}$) that sink by gravity settling to the bottom of the furnace, forming a pool of a molten iron-carbon alloy. While a thick layer of titania-rich slag floats due to its lower density above the molten iron bath. The physicochemical properties of molten titania-rich slags were described in detail elsewhere (Grau and Poggi 1978; Grau 1979) and the most salient properties are a medium density of $3500 \, \text{kg} \cdot \text{m}^{-3}$, a low dynamic viscosity of ca. 30 mPa·s quite constant at temperatures above $100°C$ of superheat (Desrosiers et al. 1980), and finally a high electronic conductivity of $6{,}500 \, \text{S} \cdot \text{m}^{-1}$. The titania-rich slag sold under the trade name Sorelslag$^{®}$ contains typically 80 mass percent TiO_2 and exhibits a particular chemistry presented in Table 8. During the slagging process, Ti^{4+} is partially reduced to Ti^{3+}, as indicated by the high Ti_2O_3 content of the bulk titania slag, while, reducible minor metal cations such as V^{3+}, Cr^{3+}, and Mn^{3+} along with some Si^{4+} are reduced partially and are distributed between the underlying molten iron layer and the titania-rich slag, the partition ratio ($K_X = a_{X,\text{metal}}/a_{X,\text{slag}}$) being strongly dependent of the reducing conditions, i.e., the oxygen fugacity ($f_O{}^{2-}$) existing inside the titania-rich melt. Actually, thermochemical considerations based on the standard Gibbs free enthalpies of formation of vanadium, chromium, and iron oxides from the elements indicate that both vanadium and chromium oxides are more thermodynamically stable than FeO and that strong reducing conditions must occur in the melt before vanadium and chromium transfer into the molten iron. Most trace elements such as cobalt and nickel follows the iron and end into the liquid metal due to their siderophilic character as indicated by the empirical formula of the iron–carbon alloy $Fe_{0.874}Co_{0.002}Ni_{0.001}Cr_{0.001}V_{0.001}Mn_{0.001}S_{0.003}C_{0.117}$ calculated from the chemical composition of the iron metal as tapped (see Table 8). Regarding the traces of sulphur coming from the anthracite coal, they combine with the volatile matter (i.e., aliphatic and aromatic hydrocarbons) and the traces of moisture to give hydrogen sulphide (H_2S) and to a lesser extend carbonyl sulphide (COS) entrained with the smelter gas and

are later trapped and removed by scrubbing. However, some remaining traces of sulphur also distribute either into the titania-rich slag or into the molten iron. Therefore, the molten iron has to be further purified by a proprietary QIT-injection process that removes all these impurities prior to be converted into high-purity pig iron (Sorelmetal$^{\circledR}$) or high-quality steel (Sorelsteel$^{\circledR}$) with the typical chemical compositions presented in Table 9.

Tapping and Cooling

The molten iron metal and titania-rich slag are tapped at regular intervals from the EAF through distinct tapholes. The titania-rich slag is poured directly into steel wagons lined with a crushed slag bedding. Afterward, the hot solidified slag blocks are cooled under water sprays for several hours in order to build a thick protective skull. They are then demoulded and stored in the field until air-cooling ensures the complete solidification of the inner core.

During air cooling, the exposed surface of the slag block undergoes characteristic disintegration or spalling due to chemical, thermal, and mechanical effects. This complex mechanism was early called decrepitation in the late 1970s at QIT and later by others (Bessinger et al. 2001; De Villiers et al. 2004).

Based on the electron microprobe analysis and the x-ray diffractogram, the major titanate phase found in the solidified Sorelslag exhibits the karrooite structure and has the average empirical chemical formula $(Fe_{0.197}Mg_{0.271}Mn_{0.004})(Ti_{1.094}Al_{0.041}V_{0.0075}Cr_{0.0025})_2O_5$, which will be explained later (Guéguin 2001). Moreover, past studies conducted on the Sorelslag using x-ray absorption near edge spectroscopy (XANES) confirmed that chromium exists as Cr^{3+} in the Sorelslag (Antonio 1989) and vanadium is also assumed to exist in the trivalent (Coetsee and Pistorius 2000) oxidation state or even lower valence states (i.e., V^{2+}). Hence, we can see that most of the titanium combines with most of the Mg^{2+} and remaining traces of Fe^{2+} to form a phase that also accommodates part of the minor metals of the ore such as Cr, V, and Al. The carbothermal reaction can then be expressed schematically as follows, highlighting the behavior of minor and trace metals:

$$(Fe, Mg, Mn)TiO_3 + (Fe, Mg)_2TiO_5$$
$$+ (Fe, Mg, Ni)(Fe, V, Al, Cr, Mn, Co)_2O_4 + C$$
$$\rightarrow (Fe, Mg, Mn)(Ti, Al, V, Cr)_2O_5 + CO + Fe(V, Mn, Cr, Ni, Co).$$
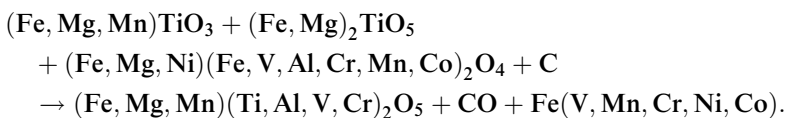
At this point, it is important to briefly describe the pseudobrookite group and its structure, which is of particular interest for understanding the mineralogy and chemistry of titania-rich slags. Minerals belonging to the pseudobrookite group exhibit the typical concise empirical chemical formula $M_xTi_{3-x}O_5$ (with $0 < x < 2$). From a crystallochemical point of view, depending on the oxidation state of the mixed valence cations and/or isomorphic substitutions, the crystal lattice can adopt the structure of one of the two end members; that is, either the karrooite structure MTi_2O_5 with $M = Mg^{2+}$, Fe^{2+} or the pseudobrookite structure *senso-stricto* originally described by Pauling (1930) M_2TiO_5 with $M = Ti^{3+}$, Fe^{3+}, Al^{3+}, V^{3+}, Cr^{3+}. Above 1320°C, it exists a continuous solid solution series (Eriksson et al. 1996) in the ternary diagram FeO-Fe_2O_3-TiO_2
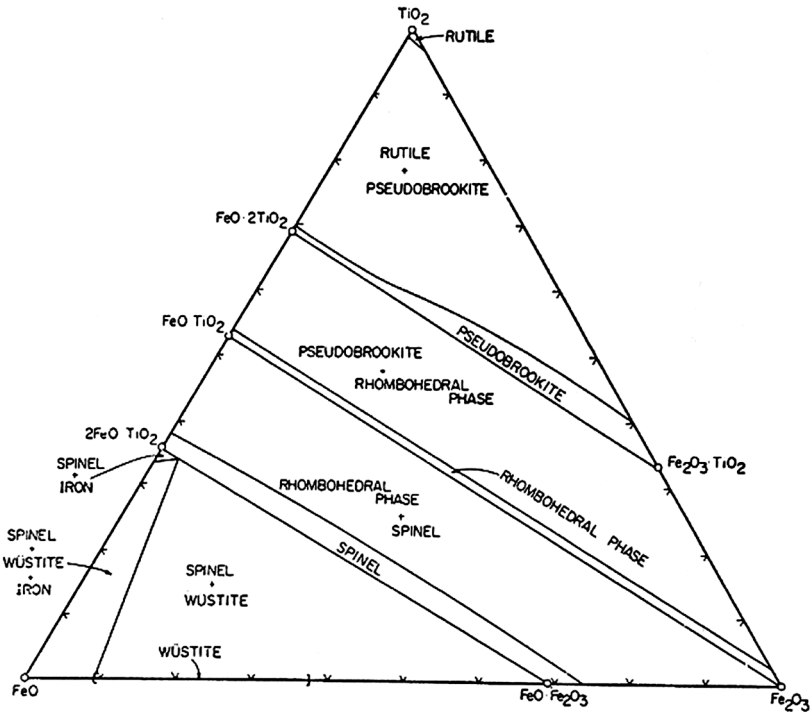
Figure 10. FeO-Fe_2O_3-TiO_2 ternary phase diagram (Taylor 1964) (reprinted by permission of the *Mineralogical Society of America*).

between pseudobrookite [1310–39-0] Fe_2TiO_5, ferro-pseudobrookite [13333-94-1] $FeTi_2O_5$, and anosovite [12065-65-5] Ti_3O_5 (see Figure 10).

Moreover, solid solutions also exists in the MgO-FeO-TiO_2 ternary diagram between anosovite, ferro-pseudobrookite, and the unnamed magnesium dititanate ($MgTi_2O_5$) with an important mineral intermediate phase called armalcolite (Anderson et al. 1970; Wechsler 1977) [13333-96-2] $(Mg_{0.75}Fe_{0.25})Ti_2O_5$ (see Figure 11).

Finally, regarding minor elements such as Cr, V, and Al: they also substitute isomorphically to Fe^{3+} in the pseudobrookite and yield the phases tialite [12004-39-6] Al_2TiO_5, berdezinskiite [85270-10-6] V_2TiO_5, and chromium pertitanate [12190-87-3] Cr_2TiO_5. Therefore, the dual pseudobrookite–karrooite structures are of peculiar importance in the chemistry and mineralogy of titania-rich slags because 1) the crystallographic sites in the crystal lattice can accommodate a variety of mixed
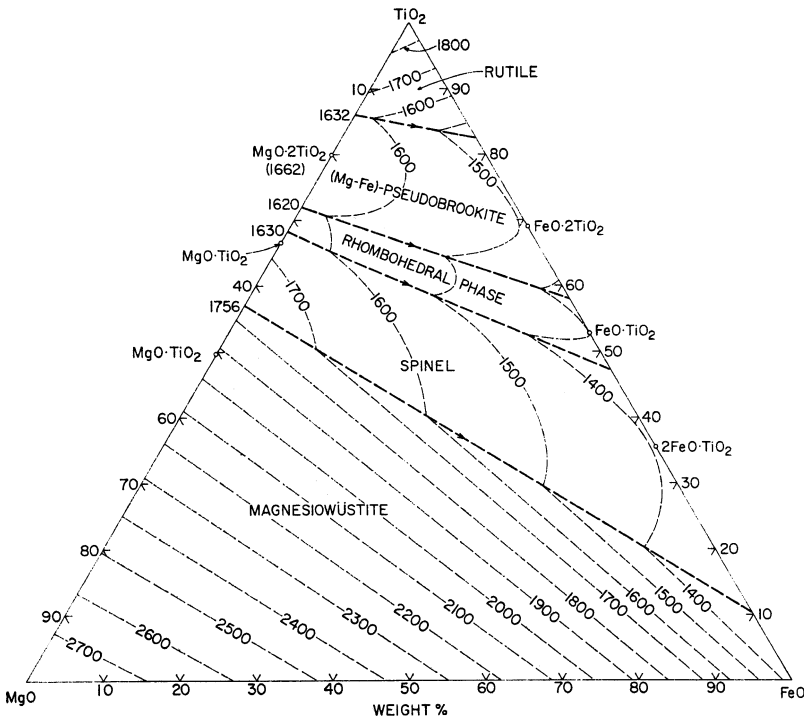
Figure 11. MgO-FeO-TiO$_2$ ternary system (Johnson et al. 1971) (reprinted by permission of the *American Journal of Science*).

valence metal cations and 2) the crystal lattice of the two end members, namely karrooite and pseudobrookite, can easily self-reorganize into each other according to the change in the oxidation state of their mixed valence cations and/or isomorphic substitutions. For information, the positions of the atoms in the two crystal lattices are summarized in Table 11.

Moreover, it is important to mention that pseudobrookite structures are metastable phases at ambient temperature. This behavior was observed in the laboratory for the pure synthetic phases such as Fe_2TiO_5 and $FeTi_2O_5$ that become unstable below $1140°C$ and $585°C$, respectively (Grey and Merritt 1981). According to Haggerty and Lindsley, pseudo-brookite decomposes into rutile and hematite below $585°C$ while ferro-pseudobrookite decomposes below $1140°C$ into rutile and hematite (Haggerty and Lindsley 1969). This was also confirmed by in situ neu-tron and x-ray diffraction studies (Teller et al. 1990b). However, the high Ti^{3+} content of titania-rich slag along with its content in minor trivalent metal cations such as Al^{3+}, V^{3+}, and Cr^{3+} stabilize the structure of the pseudobrookite at room temperature by forming solid solutions (Kesson and Lindsley 1975). A study performed on the thermal decomposition of Sorelslag shows that magnesium also increases the thermal stability of the ferro-pseudobrookite phase against further decomposition into rutile (Teller 1988). However, studies involving Mossbauer spectroscopy indi-cated that the pseudobrookite structure is distorted by these impurities

Table 11. Pseudobrookite and karrooite crystal structures

Structure	Pseudobrookite (Fe_2TiO_5)					Karrooite[**] (Mg_2TiO_5)				
Chemistry	M_2TiO_5 $M = Ti^{3+}, Fe^{3+}, Cr^{3+}, V^{3+}, Al^{3+}$					MTi_2O_5 $M = Fe^{2+}, Mg^{2+}$				
Atomic	Atom	Site	X	Y	Z	Atom	Site	X	Y	Z
position	Ti	4c	0.000	0.190	0.250	M	4c	0.0000	0.1956	0.2500
parameters	M	8f	0.000	0.135	0.560	Ti	8f	0.0000	0.1322	0.5645
(Wyckhof)	O1	4c	0.000	0.730	0.250	O1	4c	0.0000	0.7779	0.2500
	O2	8f	0.000	0.045	0.110	O2	8f	0.0000	0.0460	0.1128
	O3	8f	0.000	0.310	0.095	O3	8f	0.0000	0.3134	0.0648

References: (**)Yang H and Hazen, R. M. "Comparative high-pressure crystal chem-istry of karrooite, $MgTi_2O_5$, with different ordering states." *American Mineralogist*, 84, pp. 130–137.

(Teller et al. 1990a). Stability at high temperature has been proposed to result from mixing of cations between two different cation-oxygen octahedra, which are connected by shared edges. However, although these phases are all metastable at low temperatures, the kinetics of phase transformation into stable mixed oxides are generally so sluggish that phases such as armalcolite or karrooite may, for instance, persist for millions of years in extraterrestrial materials (e.g., lunar regolith and meteorites).

In the particular case of titania-rich slags, their high titania content above 80 wt.% TiO_2, the low-oxygen fugacity existing inside the EAF combined with the good miscibility of the various titanates at high temperature (Talmud et al. 1986) results in the formation of the previously mentioned phase: $(Fe_{0.197}Mg_{0.271}Mn_{0.004})(Ti_{1.094}Al_{0.041}V_{0.0075}Cr_{0.0025})_2O_5$ (Figure 12) that can be considered as a solid solution between armalcolite, ferro-pseudobrookite, anosovite, hongquiite (TiO), and to a lesser extent tialite, berdezinskiite, and chromium pertitanate as

$$(Fe_{0.197}Mg_{0.271}Mn_{0.004})(Ti_{1.094}Al_{0.041}V_{0.0075}Cr_{0.0025})_2O_5$$
$$= 0.0918\,Ti_{13}O_{25} + 0.361(Mg_{0.75}Fe_{0.25})Ti_2O_5$$
$$+ 0.107FeTi_2O_5 + 0.0075\,V_2TiO_5 + 0.041\,Al_2TiO_5$$
$$+ 0.004\,MnTi_2O_5 + 0.0025Cr_2TiO_5.$$
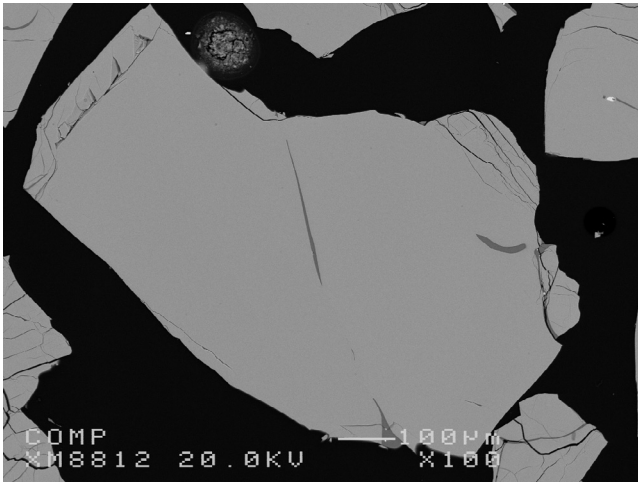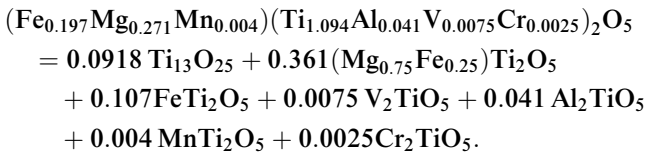
Figure 12. Sorelslag (major titanate phase with the karrooite structure).

Because the anosovite phase alone cannot account for all the excess titanium oxide remaining after combining all the metals in the above phases, the closest fit was to express the uncombined titanium oxide as $Ti_{13}O_{25}$, a well-known nonstoichiometric titanium oxide part of the Andersson–Magnelli phase series (Andersson et al. 1957) and is usually characterized by the general empirical formula Ti_nO_{2n-1} (with n > 2). This compound can also be seen as a combination of anosovite (Ti_3O_5) and hongquiite (TiO), both of which were identified in titania-rich slags in the late 1950s by Russian scientists (Veselago 1959). This compound, which was noticed for its ability to be corrosion resistant in strongly acidic solutions (Hayfield 1983), is consistent with the fact that it was already observed after the digestion in sulphuric acid of titania-rich slag. The insoluble residue yields is made of sub-stoichiometric titanium oxides and rutile (Desjardins 1986). These titanate phases are difficult to identify separately in crude titania slag, even by using x-ray diffraction (see Figure 13). But magnetic separation conducted at a high
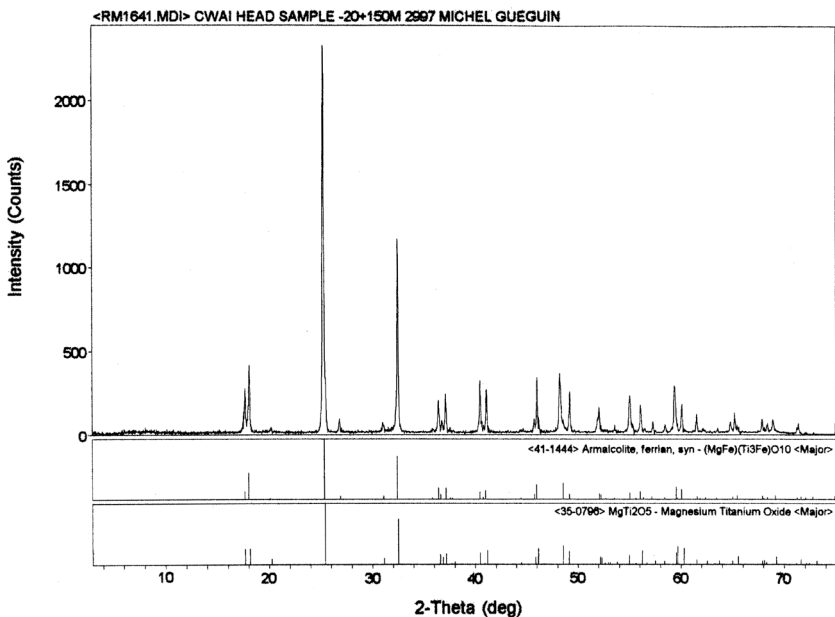
Figure 13. X-ray diffractogram of the Sorelslag (head sample).
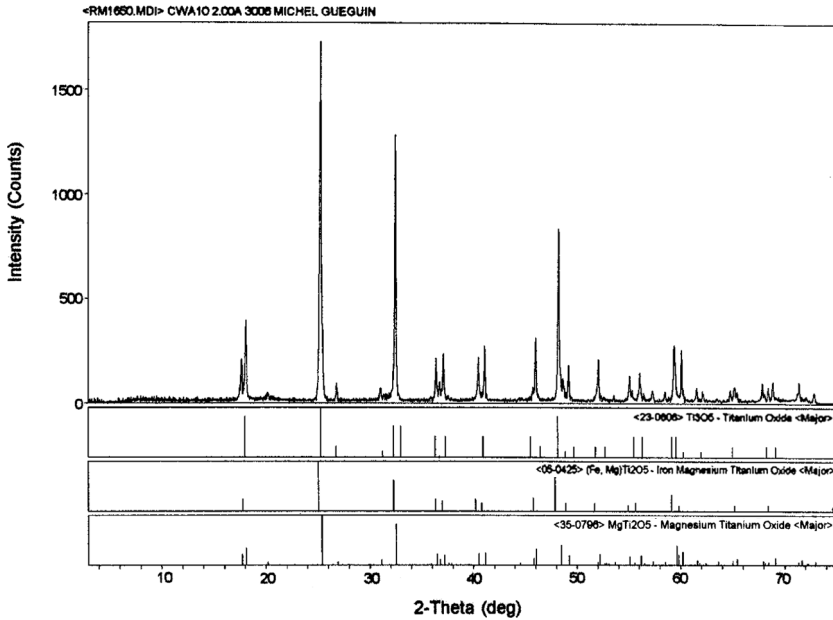
Figure 14. X-ray diffractogram of Sorelslag after magnetic separation at 0.78 T.

magnetic field induction (0.78 T) allows the concentration of anosovite, karrooite, and ferroan-pseudobrookite (Figure 14).

At that point, it is interesting to note that from 1950 until l983, when the titania content of the slag was around 74 wt.% TiO_2 the major titanate phase consisted mainly of armalcolite, a mineral discovered officially in 1969 on the Tranquility Base on the Moon and named after the acronym of the three astronauts of Apollo 11; that is, N. A. Armstrong, E. E. Aldrin, and M. Collins (Gaines et al. 1997). Moreover, it can be seen that neither vanadium nor chromium nor aluminum form distinct enriched titanates and oxides in the titania-rich slag, but they are evenly dispersed into the karrooite phase. It is important to note that if mass fraction of vanadium and chromium in the karrooite phase are considered—that is, 0.544 wt.% V_2O_3 (i.e., 0.660 wt.% V_2O_5) and 0.182 wt.% for Cr_2O_3—this seems to represent the minimum threshold concentration of these two deleterious chromophoric impurities attainable for the Sorelslag. Below these limits, the smelting conditions or the chemistry of the ore feed must be modified.

On the other hand, silica, alumina, and calcia coming mainly from the feldspar plagioclases and to a lesser extent from the ash content of the anthracite coal forms at the end of the cooling a glassy silicate phase containing traces of titanium in the form of titanite $CaTiOSiO_4$ (Guéguin 2000) with the averaged empirical formula composition is $Ca_{1.007}Ti_{0.968}Si_{0.995}O_5$ (Figure 15).

The slag also contains tiny globules of high-purity metallic iron [7439-89-6] Fe with the averaged chemical composition $Fe_{0.993}Ti_{0.006}$. For analytical and microscopical characterization purposes, these ferromagnetic tiny iron globules can be easily separated and concentrated from the bulk titania slag along with the iron sulfur troilite by magnetic separation conducted at low magnetic field induction (0.04 T). The typical x-ray diffractogram of this fraction is presented Figure 16. Usually, these tiny globules are located at the grain boundaries of the main titanate phase embedded in the silicate glassy phase (Figure 17).

Because of their high purity, it was first suggested at QIT in the 1970s and later supported and published (Toromanoff and Habashi 1984) that a redox reaction occurs in the solid state between ferrous and trivalent titanium in the pseudobrookite phase as

$$Fe^{2+} + 2Ti^{3+} \rightarrow Fe^{\circ} + 2Ti^{4+}.$$
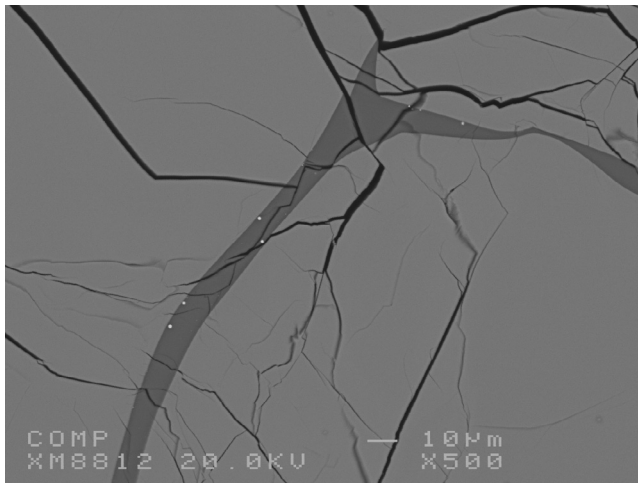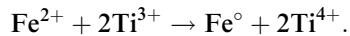
Figure 15. Sorelslag (glassy silicate phase bridging the grains of titanate and containing secondary tiny iron droplets).
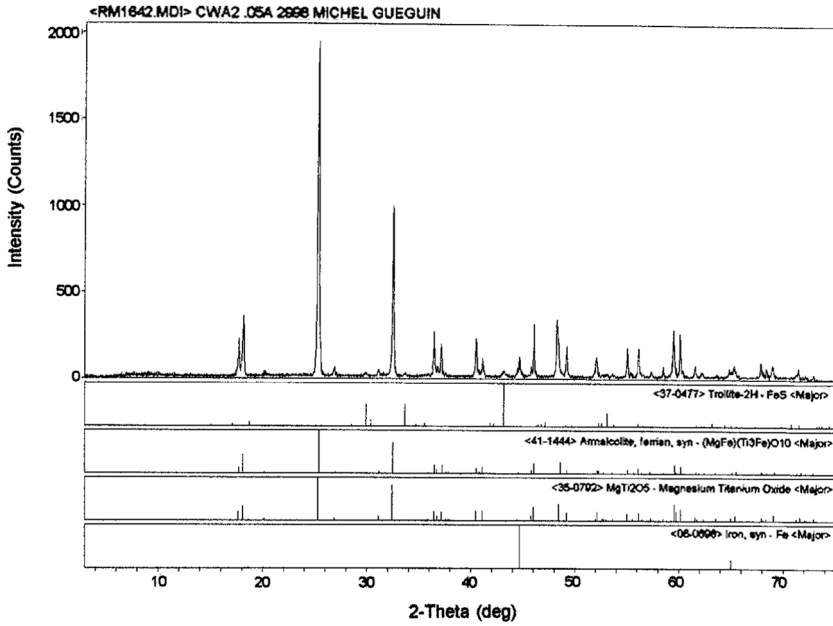
Figure 16. X-ray diffractogram of the Sorelslag after magnetic separation at 0.04 Teslas.
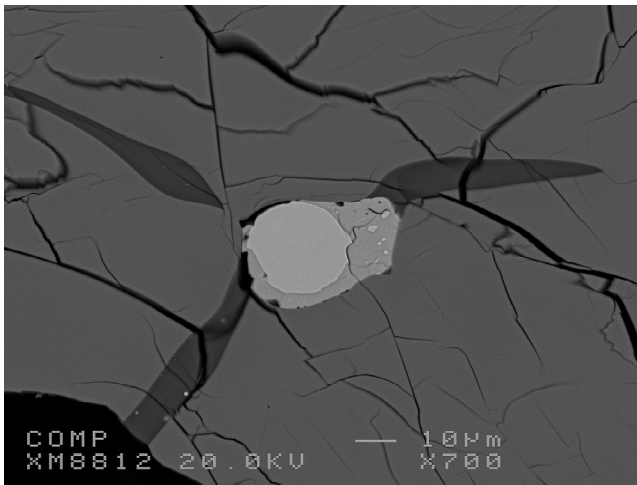
Figure 17. Sorelslag (iron droplet coated with a rim of troilite and surrounded by titanate and glassy phase).

While a smaller number of large micrometer-size globules of metallic iron are also found in the solidified titania slag comes from the entrained molten iron during tapping of the titania-rich slag. Actually, by contrast with tiny globules, they exhibit a high carbon content and traces of other impurities, as indicated by the chemical composition $Fe_{0.874}Co_{0.002}$-$Ni_{0.001}Mn_{0.001}C_{0.117}$. In all cases, either large or tiny iron globules always exhibits a rim of the rare sulphide mineral troilite [1317-96-0] FeS with the averaged chemical composition $(Fe_{1.007}Cu_{0.002})S$ that contains most of the traces of copper. This sulphide rim around iron globule was also reported in Russian's titania-rich slag (Reznichenko et al. 1981).

As mentioned in the introduction, part of Sorelslag® is sold to white pigment titanium dioxide producers worldwide to be used as a low-iron and titania-rich feedstock in the sulphate process as a substitute or in combination with ilmenite. In this process the titania-rich product is digested into sulphuric acid and precipitated, washed, dried, and calcined to yield anatase or rutile pigment. However, since 1997, a part of the production of the titania-rich slag is also further enriched using a QIT proprietary process (Borowiec et al. 2003). The novel process consists to produce an upgraded titania-rich slag (UGS®) to be used in the chloride route. This route is based on the carbochlorination of the titania for producing a titanium tetrachloride called "Ticle," which is further oxidized to yield titanium dioxide. The scope of the UGS process is to increase the titanium dioxide content and consequently to lower the level of deleterious elements such as magnesium, calcium, and iron and to a lesser extent aluminum that strongly affect the efficiency of the carbochlorination process. In order to achieve such enhancement, the titania-rich slag is crushed, sized, oxidized, reduced, acid leached, washed, and finally calcined. The chemistry and mineralogy of the intermediate products are described hereafter to understand the relationship existing between the Sorelslag and the end product; that is, the UGS. The flow sheet of the UGS process is depicted in Figure 18.

Oxidation of Sorelslag

First the crude Sorelslag is transferred to the *sizing & preparation plant* (SPP), where it undergoes crushing and screening. Afterward, the sized and ground slag is directed to the *oxidation-reduction plant* (ORP). Sorelslag undergoes a thermal oxidation performed in the oxidizer at circa 1000°C. The aim of this step is to oxidize all the Ti^{3+} into Ti^{4+} to render
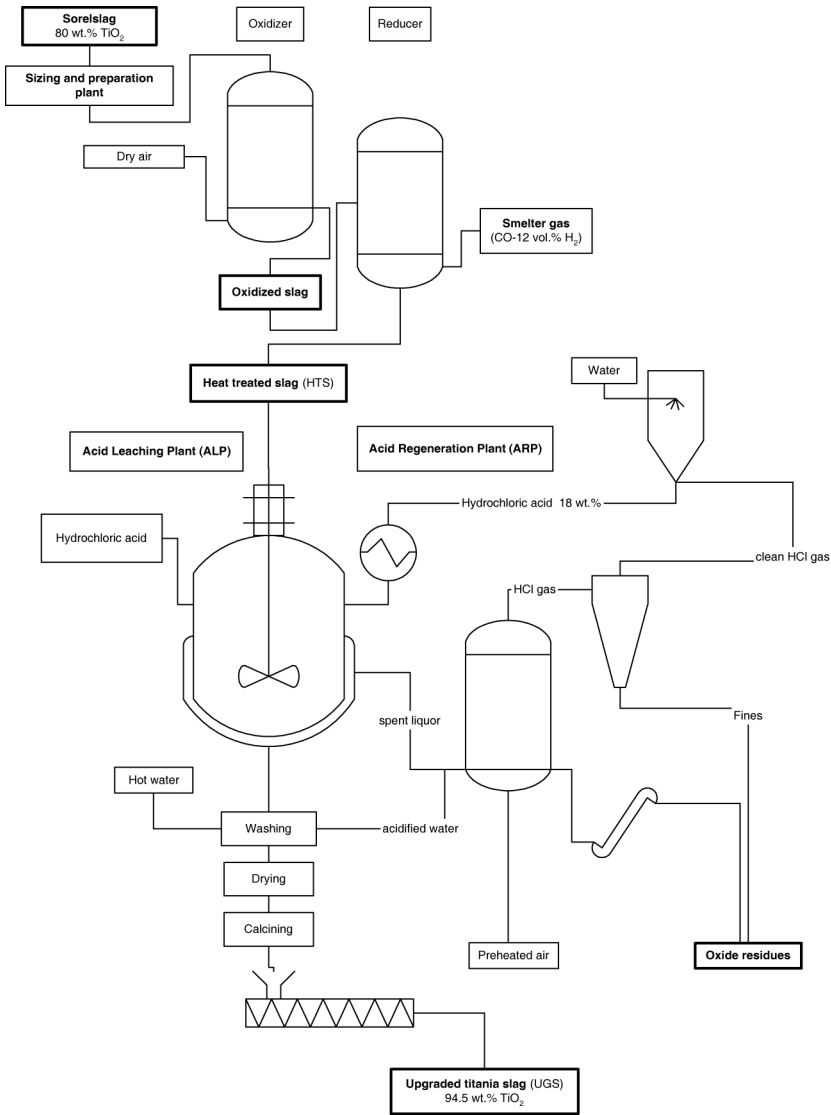
Figure 18. Upgraded titania slag process (UGS).

the titanium insoluble as titanium dioxide (TiO_2) during the subsequent high-pressure acid leaching. During this step all other reducible cations are obviously oxidized to their higher oxidation state such as Fe^{3+}, V^{5+}, and Mn^{3+}, while the Mg^{2+}, Ca^{2+}, Al^{3+}, and Cr^{3+} remain obviously unchanged.

The pseudobrookite reacts with oxygen to yield some pseudorutile [1310-39-0] $Fe_2Ti_3O_9$, $(Fe_{0.195}Ti_{0.452}V_{0.013}Mn_{0.0055}Cr_{0.005}Al_{0.073})_2Mg_{0.510}Ti_3O_9$ and ferrian rutile $(Ti_{0.994}Fe_{0.004}V_{0.002}Al_{0.001})O_2$ (Figures 19 and 20) according to the reaction of oxidation

$$2(Fe, Mg)Ti_2O_5 + 1/2O_2$$
$$\rightarrow (Fe, Ti, V, Mn, Cr, Al)_2Ti_3O_9 + (Ti, Fe, V, Al)O_2 \;\cdot$$
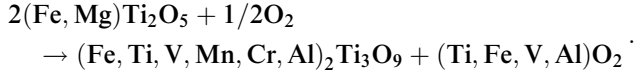
These two phases constitute mostly the oxidized slag exiting from the oxidizer (Borowiec et al. 2003). Regarding the minor element such as V^{5+}, Cr^{3+} they mainly accommodate the pseudorutile phase because they form minerals like schreyerite [60430-06-0] or kyzylkumite [80940-68-7] with the formula $V_2Ti_3O_9$ and olkhonskite [165467-07-2] $Cr_{1.5}V_{0.5}Ti_3O_9$ that form solid solution with pseudorutile. Hence, they are evenly dispersed into the crystals and no single phase containing these chromophoric elements was observed in all the studied samples.

Reduction of Oxidized Slag

The oxidized titania-rich slag undergoes a thermal reduction at $800°C$ ensured by smelter gas (i.e., $85\,vol.\%$ CO–$15\,vol.\%$ H_2). The reducing conditions existing into the reducer allows to reduce back the iron oxides
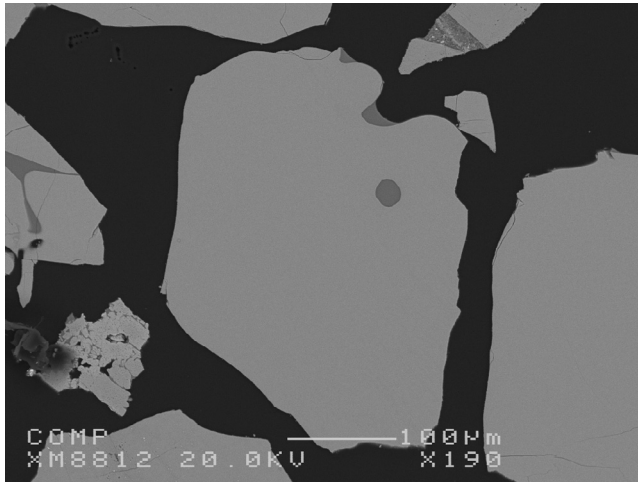
Figure 19. Oxidized titania slag (grain of pseudorutile).
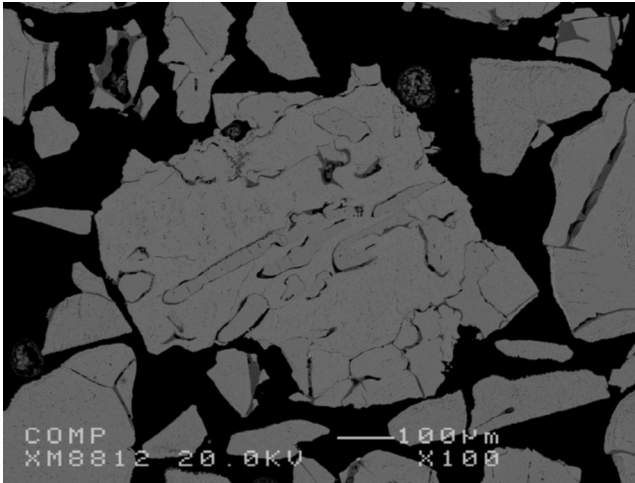
Figure 20. Oxidized titania slag (rutile grain).

into ferrous oxide while titanium dioxide remains unaffected. The resulting product called *Heat-Treated Slag* (HTS) consists mainly of a mixture of rutile $(Ti_{0.993}Fe_{0.001}V_{0.005}Al_{0.001}Cr_{0.001})O_2$ (Figure 21) and ferroan karrooite $(Fe_{0.178}Mg_{0.266}Mn_{0.006})(Ti_{1.100}Al_{0.040}V_{0.0075}Cr_{0.0025})_2O_5$.
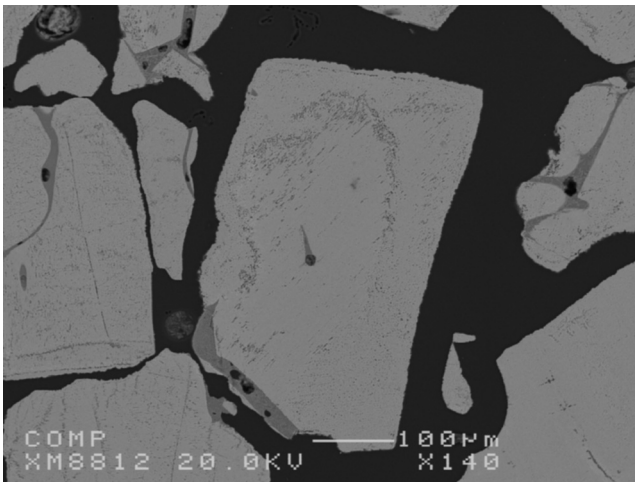
Figure 21. Heat treated titania slag (HTS) (rutile grain).

In addition, during the reduction process the iron cations initially contained into the iron-rich silicates tend to concentrate around pores, forming a thin micrometer-size layer and it also migrates to the edges of the titanate phase forming a secondary ilmenite, which is not at all related to the ilmenite originally found in the ore. For that reason, it is called *neoformed ilmenite* or simply *neo-ilmenite*.

Moreover, we can also observe that minor chromophoric elements mainly vanadium and chromium distribute evenly between the three phases, even if a slightly higher concentration exists in the rutile phase for vanadium. This dual thermal oxidation/reduction process is mandatory because it greatly enhances the acid leaching of impurities contained in the original slag with minimal consumption of hydrochloric acid values and minimal loss of titanium dioxide and without degradation of the original particle size.

High-Pressure Acid Leaching

The heat-treated titania slag exiting the reducer after cooling is sent to the *acid-leaching plant* (ALP), where it is acid leached under high pressure with an azeotropic solution of hydrochloric acid. During this step, a major part of leacheable cations such as iron, magnesium, aluminum, manganese, calcium, vanadium, and chromium are removed from the product and dissolved into the acid as metal chlorides or oxichlorides (e.g., $FeCl_2$, $MgCl_2$, $AlCl_3$, $MnCl_2$, $CaCl_2$, $VOCl_2$, and $CrCl_3$).

The leached titania-rich slag is then washed, dried, and calcined to yield the so-called upgraded titania slag (UGS) with at least 94.5 wt.% TiO_2 and less than 1.1 wt.% MgO and 0.1 wt.% CaO. Because most impurities were removed during the leaching step, the upgraded titania-rich slag is made entirely of rutile. However, examination under the electron microprobe reveals a slight difference in chemical composition existing between the core and the outside rim of the rutile grains. Rutile in the core of the grains exhibits the following averaged empirical formula $Ti_{0.896}Fe_{0.045}Mg_{0.089}Al_{0.024}V_{0.006}Cr_{0.002}Mn_{0.002}O_2$, indicating that some impurities—mostly Fe, Mg, Al, and V—are still hosted by the rutile lattice while the rutile forming rim exhibits a higher purity, as indicated by the empirical formula $Ti_{0.993}Fe_{0.003}V_{0.005}Cr_{0.001}O_2$. This can be easily understood by the fact that the hydrochloric acid has to diffuse into the grains to leach out the impurities (Figure 22). The low silica content of the UGS comes from a remaining glassy silicate phase filling the cracks
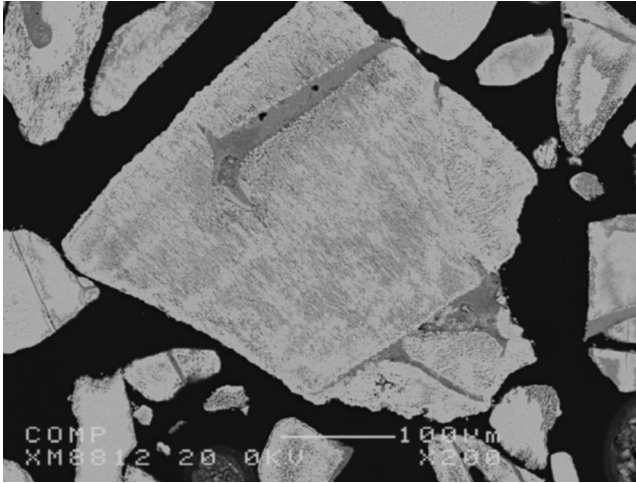
Figure 22. Upgraded titania slag (UGS) (rutile grain).

of the rutile grains (Figure 23). This amorphous solid exhibits the following composition 93.5 wt.% SiO_2, 2.9 wt.% Al_2O_3, 1.8 wt.% TiO_2, 1.1 wt.% CaO, and 0.5 wt.% Na_2O.

At the end of the process, the spent acid liquor that contains all the metal impurities as chlorides is regenerated by pyro-hydrolysis in the *acid*
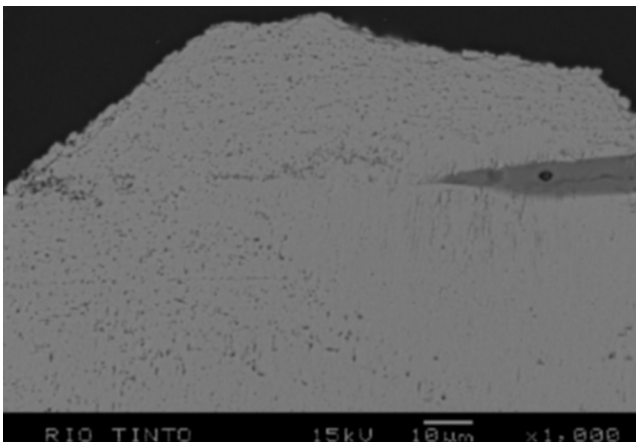
Figure 23. Upgraded titania slag (UGS) (grain of rutile with glassy silicate phase).

regeneration plant (ARP). During this process, the pyro-hydrolyzer is continuously fed with the spent acid and hot gases. The existing bed of oxides act as seed material to promote the nucleation and growth of new crystals. The process generates micrometer-size beads of metal oxides that crystallize around the previous seeds (Figure 24), and hydrogen chloride (HCl) leaves the reactor and is absorbed to yield a fresh hydrochloric acid.

Afterward, the fresh concentrated hydrochloric acid is reused upstream in the process with some make-up acid to balance the process losses and the solid oxide residues are continuously discarded. Due to a high magnesia, alumina, and ferric oxide content, the major mineral phases that form during the pyro-hydrolysis belong to the spinel group with magnesioferrite [12068-86-9] $MgFe_2O_4$ and hercynite [1302-61-0] $FeAl_2O_4$ as end-members. They usually exist as solid solution between these two end members as $Mg(Fe,Al)_2O_4$ (82 wt.%) while the excess of magnesia (9 wt.%) appears as free periclase [1309-48-44] MgO and the traces of sodium and potassium chloride form a mixed chloride $(Na_{0.8}K_{0.4}Cl)$. Most of the vanadium and chromium initially contained into the spent liquor are hosted into the above spinel minerals because they also form a solid solution as coulsonite [12418-94-9] FeV_2O_4 and chromite [1308-31-2] $FeCr_2O_4$.
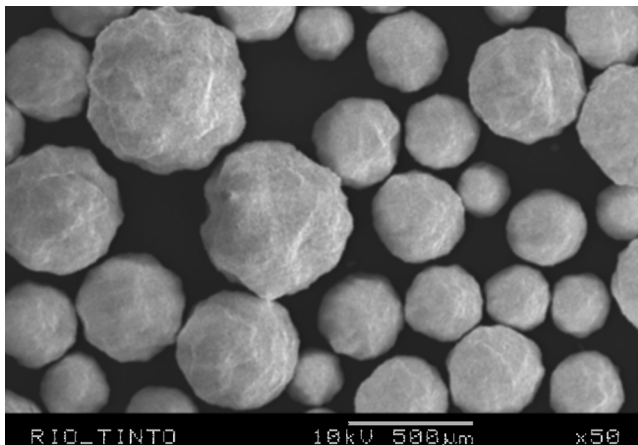
Figure 24. Acid regeneration plant (ARP) solid oxide residues.

Table 12. Properties of natural and synthetic titanate minerals identified in titania-rich slags

Mineral name [CAS RN]	IUPAC chemical formula	Structure type	Crystal system and lattice parameters	Space group (Hermann-Mauguin)	Density (kg · m^{-3})	Melting point or liquidus temperature
Anatase [1317-70-0]	TiO_2	Anatase	Tetragonal $a = 379.3$ pm $c = 951.2$ pm	$I4_1/amd$ (Z = 4)	3877	700°C (transition)
Anosovite [12065-65-5]	Ti_3O_5	Pseudobrookite	Orthorhombic $a = 374.7$ pm $b = 946.6$ pm $c = 971.5$ pm	$Bbmm$ (Z = 4)	4900	1777°C
Armalcolite [64476-39-7]	$Mg_{0.75}Fe_{0.25}Ti_2O_5$	Karrooite	Orthorhombic $a = 977.62$ pm $b = 1002.14$ pm $c = 374.85$ pm	$Bbmm$ (Z = 4)	3904	1550°C
Berdesinskiite [85270-10-6] (Bernhardt et al. 1981, 1983)	V_2TiO_5	Pseudobrookite	Monoclinic $a = 1011$ pm $b = 508.4$ pm $c = 703$ pm $\beta = 111.46°$	$Bbmm$ (Z = 4)	4540	1750°C
Brookite [12188-41-9]	TiO_2	Brookite	Orthorhombic $a = 545.6$ pm $b = 918.2$ pm $c = 514.3$ pm	$Pbca$ (Z = 8)	4130	1900°C

(*Continued*)

45

Table 12. Continued

Mineral name [CAS RN]	IUPAC chemical formula	Structure type	Crystal system and lattice parameters	Space group (Hermann-Mauguin)	Density (kg · m^{-3})	Melting point or liquidus temperature
Cafetite [12414-42-5] (Kukharenko et al. 1959) (Krivovichev et al. 2003)	$CaTi_2O_5 \cdot H_2O$	Karrooite	Monoclinic $a = 494.36$ pm $b = 1210.9$ pm $c = 15911$ pm $\beta = 98.937°$	P2$_1$/n Z = 8	3280	
Calcium dititanate [12013-80-8] (Elcombe et al. 1991)	$Ca_3Ti_2O_7$	Ruddlesden-Popper ($A_{n+1}B_nX_{3n+1}$)	Orthorhombic $a = 541.72$ pm $b = 1951.69$ pm $c = 542.34$ pm	Ccm21 (Z = 4)		1740°C
Chromium dititanate [12013-80-8] (Mueller et al. 1988)	$CrTi_2O_5$	Karrooite	Monoclinic $a = 1005.01$ pm $b = 502.72$ pm $c = 706.32$ pm $\beta = 111.61°$	C2/c Z = 4		
Chromium pertitanate [12190-87-3] (Kamiya et al. 1979)	Cr_2TiO_5	Pseudobrookite	Monoclinic $a = 702.0$ pm $b = 5025$ pm $c = 994.5$ pm $\beta = 111.43°$	Bbmm (Z = 4)		
Ferro-pseudobrookite [12449-79-5] (Simons and Woermann 1978)	$FeTi_2O_5$	Karooite	Monoclinic	A2/m		1500°C

Mineral [CAS] (Reference)	Formula	Structure	Crystal system / space group and lattice parameters		
Geikielite [9312-99-8]	$MgTiO_3$	Ilmenite	Trigonal *R3* (Z = 6), $a = 508.6$ pm, $c = 1409.3$ pm	3790	1630°C
Ilmenite [12168-52-4] (Wechsler and Prewitt 1984)	$FeTiO_3$	Ilmenite	Trigonal *R3* (Z = 6), $a = 508.84$ pm, $c = 1408.85$ pm	4786	1470°C
Karrooite [12032-35-8] (Yang and Hazen 1999)	$MgTi_2O_5$	Karrooite	Orthorhombic *Cmcm* (Z = 4), $a = 373.85$ pm, $b = 971.87$ pm, $c = 1000.25$ pm	3630	1690°C
Kassite [61159-21-5] (Evans et al. 1986)	$CaTi_2O_4(OH)_2$	Kassite	Monoclinic P2$_1$/a (Z = 8), $a = 527.5$ pm, $b = 900.9$ pm, $c = 955.7$ pm, $\beta = 90.43°$	3280	
Kyzylkumite [80940-68-7] (Smyslova 1981)	$V_2Ti_3O_9$	Pseudorutile	Monoclinic (Z = 4), $a = 3380$ pm, $b = 457.8$ pm, $c = 1999$ pm, $\beta = 93.40°$	3770	
Magnesium dititanate [65405-38-1] (Titan GmbH 1939) (Isobe 2002)	$MgTi_2O_4$	Spinel	Cubic $a = 860$ pm *Fd3m*		

(Continued)

Table 12. Continued

Mineral name [CAS RN]	IUPAC chemical formula	Structure type	Crystal system and lattice parameters	Space group (Hermann-Mauguin)	Density $(kg \cdot m^{-3})$	Melting point or liquidus temperature
Manganese orthotitanate [12032-93-8] (Grey et al. 1976)	Mn_2TiO_4	Spinel	Cubic	$Fd3m$		1450°C
No name No name (Matsumoto 1972)	$Mg_2Ti_3O_9$ $Ca_4Ti_3O_{10}$	Pseudorutile	Orthorhombic $a = 540.83$ pm $b = 2714.32$ pm $c = 543.37$ pm	$Pbca$ (Z = 4)		1755°C
Olkhonskite [165467-07-2] (Koneva et al. 1994, 1995)	$Cr_{1.5}V_{0.5}Ti_3O_9$	Pseudorutile	Monoclinic $a = 703$ pm $b = 502$ pm $c = 1883$ pm $\beta = 119.6°$	(Z = 4)	4480	
Perovskite [12049-50-2]	$CaTiO_3$	Perovskite	Orthorhombic $a = 536.70$ pm $b = 544.39$ pm $c = 764.38$ pm	$Pbnm$	4044	1970°C
Pseudobrookite [1310-39-0]	Fe_2TiO_5	Pseudobrookite	Orthorhombic $a = 976.7$ pm $b = 994.7$ pm $c = 371.7$ pm	$Bbmm$ (Z = 4)	4406	1375°C

Name [CAS] (Ref.)	Formula	Structure type	Crystal system	Space group	Density	Temperature
Pseudorutile [1310-41-4] (Grey and Reid 1975)	$Fe_2Ti_3O_9$	Pseudorutile	Trigonal $a = 1437.5$ pm $c = 461.5$ pm	$P3_22$ ($Z = 5$)	4010	
Pyrophanite [12032-74-5]	$MnTiO_3$	Ilmenite	Trigonal $a = 513.7$ pm $c = 1428.3$ pm	$R3$ ($Z = 6$)	4603	1360°C
Qandilite [12032-52-9] (Stubicar et al. 2004)	Mg_2TiO_4	Spinel	Cubic $a = 844$ pm	$Fd3m$	4040	1732°C
Rutile [1317-80-2]	TiO_2	Rutile	Tetragonal $a = 459.37$ pm $c = 296.18$ pm	$P4_2/mnm$ ($Z = 2$)	4274	1847°C
Schreyerite [60430-06-0] (Medenbach and Schmetzer 1978; Bernhardt et al. 1983)	$V_2Ti_3O_9$	Pseudorutile	Monoclinic $a = 706$ pm $b = 501$ pm $c = 1874$ pm $\beta = 119.4°$	($Z = 4$)	4480	1740°C
Tialite [12004-39-6]	Al_2TiO_5	Pseudobrookite	Orthorhombic $a = 942.9$ pm $b = 963.6$ pm $c = 359.1$ pm	$Bbmm$ ($Z = 4$)	3702	1860°C
Ulvospinel [12063-18-2]	Fe_2TiO_4	Spinel	Cubic $a = 853.6$ pm	$Fd3m$	4780	
Vanadium dititanate	$V_2Ti_2O_7$	Pyrochlore				

Table 13. Titanates and polytitanates crystal structures

Group	Subgroup	Chemical formula	Metal cations type (Coordination No.)	Natural or synthetic mineral	
Monotitanates	Metatitanates ($MTiO_3$)				
	Ilmenite structure	$MTiO_3 = M^{II}O \cdot TiO_2$	$M(6) = Fe^{2+}, Mg^{2+}, Mn^{2+}$ Ti(6) M^{2+} same radius as Ti^{4+}	Ilmenite Pyrophanite Geikielite	$FeTiO_3$ $MnTiO_3$ $MgTiO_3$
	Perovskite structure	$MTiO_3 = M^{II}O \cdot TiO_2$	$M(12) = Ca^{2+}, Ba^{2+}, Sr^{2+}$ Ti(6) M^{2+} greater radius than Ti^{4+}	Perovskite Tausonite Ba metatitanate	$CaTiO_3$ $SrTiO_3$ $BaTiO_3$
	Orthotitanates (M_2TiO_4)				
	Spinel structure	$M_2TiO_4 = 2M^{II}O \cdot TiO_2$	$M(4) = Fe^{2+}, Mg^{2+}, Mn^{2+}$ Ti(6) M^{2+} same radius as Ti^{4+}	Ulvospinel Qandilite Mn ortho-titanate	Fe_2TiO_4 Mg_2TiO_4 Mn_2TiO_4
	Pertitanates (M_2TiO_5)				
	Pseudobrookite structure	$M_2TiO_5 = M^{III}_2O_3 \cdot TiO_2$	$M = Fe^{3+}, Al^{3+}, Mn^{3+}$ $(Cr^{3+}, V^{3+}, Ti^{3+})$ Ti(6)	Pseudobrookite Tialite Berdesinskiite Cr-pertitanate Anosovite	Fe_2TiO_5 Al_2TiO_5 V_2TiO_5 Cr_2TiO_5 Ti_3O_5

	Structure	Formula	M	Mineral	Compound
Dititanates	Karrooite structure	$MTi_2O_5 = M^{II}O \cdot 2TiO_2$	$M = Fe^{2+}, Mg^{2+}, Mn^{2+}$ Ti(6)	Ferropseudobrookite Armalcolite Karrooite Cafetite	$FeTi_2O_5$ $Mg_{0.75}Fe_{0.25}Ti_2O_5$ $MgTi_2O_5$ $CaTi_2O_5 \cdot H_2O$
	Pyrochlore structure with M(II)	$M_3Ti_2O_7 = 3M^{II}O \cdot 2TiO_2$	$M = Ca^{2+}, Sr^{2+}, Ba^{2+}$ M^{2+} greater radius than Ti^{4+}	(no name)	$Ca_3Ti_2O_7$
	Pyrochlore structure with M(III)	$M_2Ti_2O_7 = M^{II}_2O_3 \cdot 2TiO_2$	$M = Fe^{3+}, Al^{3+}, Mn^{3+}$ $(Cr^{3+}, V^{3+}, Ti^{3+})$ Ti(6)	(no name)	$V_2Ti_2O_7$
Trititanates	Pseudorutile structure	$M_2Ti_3O_9 = M^{III}_2O_3 \cdot 3TiO_2$	$M = Fe^{3+}, Al^{3+}, Mn^{3+}$ $(Cr^{3+}, V^{3+}, Ti^{3+})$ Ti(6)	Pseudorutile Schreyerite Kyzylkumite Olkhonskite	$Fe_2Ti_3O_9$ $V_2Ti_3O_9$ $V_2Ti_3O_9$ $Cr_{1.5}V_{0.5}Ti_3O_9$
		$AB_2Ti_3O_9$ $= A^{II}O \cdot B^{III}_2O_3 \cdot 3TiO_2$	$A = Fe^{2+}, Mg^{2+}, Mn^{2+}$ $B = Fe^{3+}, Al^{3+}, Mn^{3+}$ $(Cr^{3+}, V^{3+}, Ti^{3+})$ Ti(6)	(no name)	$Fe_3Ti_3O_{10}$

CONCLUSIONS

In this comprehensive study, based on microchemical analysis combined to x-ray diffraction, we have shown that titania-rich slags produced from the smelting of hemo-ilmenite ore with anthracite coal and related products exhibits a chemistry and mineralogy unique among other natural and man-made materials. This remarkable difference is essentially due the elevate titania content of the materials combined with the extremely high temperatures involved during the metallurgical processing that leads to the formation of rare titanates phases. Most of them belonging to the pseudobrookite–karrooite group. The most important results and observations are as follows.

1) The major phase in the Sorelslag exhibits the empirical chemical formula $(Fe_{0.197}Mg_{0.271}Mn_{0.004})(Ti_{1.094}Al_{0.041}V_{0.0075}Cr_{0.0025})_2O_5$ with a karrooite type structure. This structure is of peculiar importance in titania-rich slags because its crystal lattice can accommodate a wide variety of mixed valence metal cations. In the case of titania slag, the structure host most of the deleterious and chromophoric metal impurities, especially iron, manganese, vanadium, and chromium that always form compounds in solid solution into the titanate phase and were never found as single rich titanate, oxide, or silicate phase.

2) The major titanate phase in the Sorelslag can be seen as a solid solution of various titanates (i.e., armalcolite, ferropseudobrookite, tialite, V_2TiO_5, and Cr_2TiO_5) all with the pseudobrookite–karrooite structure and the excess titanium oxide, which is not chemically combined forms a nonstoichiometric oxide with the empirical formula $Ti_{13}O_{25}$ part of the Andersson–Magneli phases. This highly corrosion resistant compound is consistent with the fact that it was also observed in the insoluble residue after digestion of Sorelslag in sulphuric acid and to a lesser extent to the good electronic conductivity of the titania-rich slags either in the solid or molten state.

3) The removal of impurities from the Sorelslag by a proprietary hydrometallurgical process yields the purest synthetic rutile on the market, which is suitable for the chloride route for producing titanium dioxide pigment.

4) Regarding minor elements, neither vanadium nor chromium were observed as single titanate or oxide V_2O_5 nor Cr_2O_3 in the QIT

products, but they were always detected as solid solutions inside the other titanate or oxide phases.

APPENDICES

See Tables 12 and 13.

REFERENCES

Andersson, S., Collen, B., Kuylenstierna, U., and Magneli, A., 1957, "Phase analysis studies of the titanium-oxygen system." *Acta. Chemica. Scandinavia*, 11, pp. 1641.

Anderson, A. T., Cameron, E. N., Haggerty, S. E., Boyd, F. R., Finger, L. W., James, O. B., Keil, K., Prinz, M., Ramdohr, P., and Goresy, A. E., 1970, "Armalcolite: A new mineral from the Apollo 11 samples." *Apollo 11 Lunar Conference Proceedings*, 1, pp. 55–63.

Antonio, M. R., 1989, "Valence of chromium in slags and digestion residues," Analytical Report No. 756, Project #14050-02, BP America Research & Development Structural Analysis, Analytical and Environmental Sciences, Warrensville, OH, August 15.

Bergeron, M., 1986, "*Minéralogie et géochimie de la suite anorthositique de la région du Lac Allard Québec: Évolution des membres mafiques et origine des gîtes d'ilménite*," Ph.D. Thesis, Université de Montréal, École Polytechnique.

Bergeron, M. and Priest, S. F., 1976, "Magnetic separation of ilmenite," *US Patent* 3,935,094, January 27.

Bernhardt, H.-J., Schmetzer, K., and Medenbach, O., 1981, "Berdesinskiit—V_2TiO_5, ein neues mineral." *Zeitschrift der deutschen Gemmologischen Gesellschaft*, 30, pp. 143–145.

Bernhardt, H.-J., Schmetzer, K., and Medenbach, O., 1983, "Berdesinskiite, V_2TiO_5, a new mineral from Kenya and additional data for schreyerite, $V_2Ti_3O_9$." *Neues Jahrbuch für Mineralogie, Monatshefte*, March, pp. 110–118.

Bessinger, D., Geldenhuis, J. M. A., Pistorius, P. C., Mulaba, A., and Hearne, G., 2001, "The decrepitation of solidified high titania slags." *Journal of Non-Crystalline Solids*, 282, pp. 132–142.

Borowiec, K., Grau, A. E., Guéguin, M., and Turgeon, J.-F., 1998, "Method to upgrade titania slag and resulting product," *US Patent* 5,830,420, November 3.

Borowiec, K., Grau, A. E., Guéguin, M., and Turgeon, J.-F., 2003, "TiO_2 containing product including rutile, pseudo-brookite and ilmenite," *US Patent* 6,531,110, March 11.

Briggs, R. A. and Sacco, A., Jr., 1993, "The oxidation of ilmenite and its relationship to the ferrous oxide-ferric oxide-titania phase diagram at 1073 and 1140 K." *Metallurgical Transactions A: Physical Metallurgy and Materials Science*, 24A(6), pp. 1257–1264.

Chase, M. W., Jr., 1998, "NIST-JANAF thermochemical tables, part. I and II," *Physical and Chemical Reference Data, Monograph No. 9*, 4th Ed., New York: Springer.

Coetsee, T. and Pistorius, C., 2000, "Preliminary observations on phase relations in the V_2O_3-FeO and V_2O_3-TiO_2 systems from $1400°C$ to $1600°C$ in reducing atmospheres." *Journal of the American Ceramic Society*, 83(6), pp. 1485–1488.

Cui, Z., Liu, Q., and Etsell, T. H., 2002, "Magnetic properties of ilmenite, hematite and oil sand minerals after roasting." *Minerals Engineering*, 15, pp. 1121–1129.

Desjardins, J.-F., 1986, "Study of the insoluble in Richards bay slag," QIT Internal Report R-11–86.

Desrosiers, R., Ajersch, F., and Grau, A. E., 1980, "Electrical conductivity of industrial slags of high titania content," Proceedings International Symposium on Metallurgical Slags, Part of the 19th Annual Conference of Metallurgists, Halifax, Nova Scotia, Canada, August 24–27.

De Villiers, J. P. R., Verryn, S. M. C., and Fernandes, M. A., 2004, "Disintegration in high-grade titania slags: Low temperature oxidation reactions of ferro-pseudobrookite." *Mineral Processing and Extractive Metallurgy* (*Trans. Inst. Mining Metall. C*), 113, pp. C66–C74.

Donald, H. L., 1976, "The crystal chemistry and structure of oxide minerals as exemplified by the Fe-Ti oxides," In *Oxides Minerals. Short Course Notes*, Vol. 3. (D. Rumble III, Ed.), Washington, DC: Mineralogical Society of America, pp. Hg1–Hg100.

Elcombe, M. M., Kisi, E. H., Hawkins, K. D., White, T. J., Goodman, P., and Matheson, S., 1991, "Structure determinations for $Ca_3Ti_2O_7$, $Ca_4Ti_3O_{10}$, $Ca_{3.6}Sr_{0.4}Ti_3O_{10}$ and a refinement of $Sr_3Ti_2O_7$." *Acta. Crystallographica*, B47, pp. 305–314.

Eriksson, G., Pelton, A. D., Woermann, E., and Ender, A., 1996, "Measurement and thermodynamic evaluation of phase equilibria in the Fe-Ti-O system." *Ber. Bunsenges. Phys. Chem.*, 100, pp. 1839–1849.

Evans, H. T., Dwornik, E. J., and Milton, C., 1986, "Kassite from the diamond jo quarry, magnet cove, hot spring county, Arkansas: The problem of cafetite and kassite." *American Mineralogist*, 71(7–8), pp. 1045–1048.

Forman, S. A., Prince, A. T., and Bright, N. F. H., 1954, "The separation and identification of the titanoferous and siliceous constituents of slag from the Quebec Iron & Titanium Corporation," Research Report No. MD169,

Canada Department of Mines and Technical Surveys Mines Branch (CANMET), Ottawa, ON, Canada.

Gaines, R. V., Skinner, H. C. W., Foord, E. E., Mason, B., and Rosenzweig, A., 1997, *Dana's New Mineralogy: The System of Mineralogy of James Dwight Dana and Edward Salisbury Dana*, 8th Ed., New York: Wiley-Interscience.

Grau, A. E. and Poggi, D., 1978, "Physico-chemical properties of molten titania slags." *Canadian Metallurgical Quarterly*, 17, pp. 97–102.

Grau, A. E., 1979, "Liquidus temperature in the TiO_2-rich side of the FeO-TiO_2 systems." *Canadian Metallurgical Quarterly*, 18, pp. 313–321.

Grey, I. E., Li, C., and Reid, A. F., 1976, "Phase equilibria in the system MnO-TiO_2-Ti_2O_3 at 1473 K." *Journal of Solid State Chemistry*, 17(4), pp. 343–352.

Grey, I. E. and Merritt, R. R., 1981, "Stability relations in the pseudobrookite solid solution $Fe_yTi_{3-y}O_5$." *Journal of Solid State Chemistry*, 37, pp. 284–293.

Grey, I. E. and Reid, A. F., 1975, "The structure of pseudorutile and its role in the natural alteration of ilmenite." *American Mineralogist*, 60, pp. 898–906.

Guéguin, M., 1972, "Upgrading Sorelslag. Preliminary Results on Magnetic Separation Tests," QIT Internal Report R-29-1972.

Guéguin, M., 2000, "Phases de la scorie près de la cavité dans un bloc," RIT Internal Report R-33-2000.

Guéguin, M., 2001, "Scorie de coin de bloc," RIT Internal Report R-15-2001.

Guéguin, M., 2004a, "Séparation magnétique de la Sorelslag décrépitée. Composition, diffraction et étude SEM/EDS des fractions granulométriques," RIT Internal Report R-04-2004.

Guéguin, M., 2004b, "Beneficiation of titaniferous slags," *PCT International Patent Application WO 2004/104239*, December 2.

Guimond, R., 1964, "Titanium and QIT." *Mining in Canada*, 11, pp. 11–23.

Haggerty, S. E., 1976, "Oxidation of opaque mineral oxides in basalts," In *Oxides Mineals. Short Course Notes*, Vol. 3. (D. Rumble III, Ed.), Washington, DC: Mineralogical Society of America, pp. Hg1–Hg100.

Haggerty, S. E. and Lindsley, D. H., 1969, *Carnegie Institution Washington Yearbook*, 68, p. 247.

Hammond, P., 1952, "Allard lake ilmenite deposits." *Economic Geology*, 47, pp. 634–649.

Hayfield, P. C. S., 1983, "Electrode material, electrode and electrochemical cell," *US Patent* 4,422,917, December 27.

Isobe, M., 2002, "Observation of phase transition from metal to spin-singlet insulator in $MgTi_2O_4$ with $S = 1/2$ pyrochlore lattice." *Journal of the Physical Society of Japan*, 71(8), pp. 1848–1851.

Johnson, R. E., Woermann, E., and Muan, A., 1971, "Equilibrium studies in the system magnesium oxide-iron oxide-titanium oxide." *American Journal of Science*, 271(3), pp. 278–292.

Kamiya, S., Hirano, S., and Somiya, S., 1979, "The compound Cr_2TiO_5 in the system Cr_2O_3-TiO_2." *Solid State Chemistry*, 28, pp. 21–28.

Kesson, S. E. and Lindsley, D. H., 1975, "The effect of Al^{3+}, Cr^{3+}, and Ti^{3+} on the stability of armalcolite," Proceedings of the Sixth Lunar Science Conference, Geochimica and Cosmochimica Acta, Suppl. 6, pp. 911–920.

Koneva, A. A., Piskunova, L. F., Ushchapovskaya, Z. F., and Konev, A. A., 1994, "Olkhonskite $(Cr,V)_2Ti_3O_9$—A new mineral from Priol'khonie (Russia)." *Zapiski Vserossiiskogo Mineralogicheskogo Obshchestva*, 123(4), pp. 98–103.

Koneva, A. A. and Suvorova, L. F., 1995, "Rare chromium and vanadium oxides in metamorphic rocks of Priol'khonye (Lake Baikal area)." *Zapiski Vserossiiskogo Mineralogicheskogo Obshchestva*, 124(4), pp. 52–61.

Krivovichev, S. V., Yakovenchuk, V. N., Burns, P. C., Pakhomovsky, Y. A., and Menshikov, Y. P., 2003, "Cafetite: Crystal structure and revision of chemical formula." *American Mineralogist*, 88(2–3), pp. 424–429.

Kukharenko, A. A., Kondrat'eva, V. V., and Kovyazina, V. M., 1959, "Cafetite, a new hydrated calcium-iron titanate." *Zapiski Vserossiiskogo Mineralogicheskogo Obshchestva*, 88, pp. 444–453.

Lethuillier, P. and Massal, P., 1980, "Propriétés magnétiques de grenats et d'ilménites naturels prélevés dans des gisements variés." *Bulletin de Minéralogie*, 103(1), pp. 33–39.

Mandelbrot, B., 1986, "Comment j'ai decouvert les fractales." *La Recherche*, November, pp. 420–424.

Matsumoto, O., Ishida, K., and Mitsuya, Y., 1972, "Study of oxide systems by means of the arc imaging furnace. I. Phases found in quenched specimens of the titanium dioxide-calcium oxide system." *Denki Kagaku*, 40(9), pp. 641–645.

Medenbach, O. and Schmetzer, K., 1978, "Schreyerite, $V_2Ti_3O_9$, a new mineral." *American Mineralogist*, 63(11–12), pp. 1182–1186.

Mueller-Buschbaum, H. and Bluhm, K., 1988, "Additional magnetic examinations of titanium ternary oxides ($Ti_{3-x}M_xO_5$-phases (M = Al^{3+}, Fe^{2+}, Mn^{2+}, Mg^{2+}) with a contribution about chromium titanium oxide ($CrTi_2O_5$)." *Zeitschrift fur Anorganische und Allgemeine Chemie*, 558, pp. 28–34.

Pauling, L., 1930, "The crystal structure of pseudobrookite." *Z. Kristallogr.*, 73, pp. 97–112.

Peirce, W. M., Waring, R. K., and Fetterolf, D. L., 1949, "Titaniferous material for producing titanium dioxide," *US Patent* 2,476,453, July 19.

Reznichenko, V. A., Karyazin, I. A., Il'yashenko, S. F., and Olyunina, T. V., 1981, "Metallic inclusions in high-titanium slags." *Russian Metallurgy*, 4(1–2), pp. 16–20.

Robinson, P., Panish, P. T., and McEnroe, S. A., 2001, "Minor element chemistry of hemo-ilmenite and magnetite in cumulate rocks from the Sokndal region, South Rogaland, Norway." *American Mineralogist*, 86, pp. 1469–1476.

Shirane, G., Cox, D. E., Takei, W. J., and Ruby, S. L., 1962, "A study of magnetic properties of the $FeTiO_3$—a-Fe_2O_3, system by neutron diffraction and Mossbauer effect." *Journal of the Physical Society of Japan*, 17(10), pp. 1598–1611.

Simons, B. and Woermann, E., 1978, "Iron titanium oxides in equilibrium with metallic iron." *Contributions to Mineralogy and Petrology*, 66(1), pp. 81–89.

Smyslova, I. G., Komkov, A. I., Pavshukov, V. V., and Kuznetsova, N. V., 1981, Kyzylkumite, $V_2Ti_3O_9$ as a new mineral from a group of complex vanadium and titanium oxides." *Zapiski Vsesoyuznogo Mineralogicheskogo Obshchestva*, 110(5), pp. 607–612.

Stubicar, N., Tonejc, A., and Stubicar, M., 2004, "Microstructural evolution of some MgO-TiO_2 and MgO-Al_2O_3 powder mixtures during high-energy ball milling and post-annealing studied by x-ray diffraction." *Journal of Alloys and Compounds*, 370(1–2), pp. 296–301.

Talmud, N. I., Reznichenko, V. A., Model, M. S., Olyunina, T. V., and Naumova, L. O., 1986, "Reciprocal solubility of iron titanate ($FeTi_2O_5$) and magnesium titanate ($MgTi_2O_5$)." *Izvestiya Akademii Nauk SSSR, Neorganicheskie Materialy*, 22(10), pp. 1750–1751.

Taylor, R. W., 1964, "Phase equilibriums in the system FeO-Fe_2O_3-TiO_2 at $1300°C$." *American Mineralogist*, 49(7–8), pp. 1016–1030.

Teller, R. G., 1988, "High temperature x-ray diffraction study of the thermal decomposition of two pseudobrookite compounds $Fe_{0.9}Ti_{2.1}O_5$ and $Mg_{0.6}Fe_{0.3}Ti_{2.1}O_5$," Topical Report No. 7777, Project No. 8573, BP America Research & Development Structural Analysis, Analytical and Environmental Sciences, Warrensville, OH, February 23.

Teller, R. G., Antonio, M. E., Grau, A., Gueguin, M., and Kostiner, E., 1990a, "Structural analysis of metastable pseudobrookite ferrous titanium oxides with neutron diffraction and mossbauer spectroscopy." *Journal of Solid. State Chemistry*, 88, pp. 334–350.

Teller, R. G., Antonio, M. E., Grau, A., Gueguin, M., and Kostiner, E., 1990b, "The chemistry of the thermal decomposition of pseudobrookite ferrous titanium oxides." *Journal of Solid. State Chemistry*, 88, pp. 351–367.

Titan, GmbH, 1939, "Process for the manufacture of magnesium-titanium-spinel," *Great Britain Patent* 498,904, January 13.

Toromanoff, I. and Habashi, F., 1984, "The composition of slag from Sorel." *Journal of Less Common Metals*, 97, pp. 317–329.

Veselago, L. I., 1959, "Determination of bivalent and trivalent titanium in slags containg metallic iron and ferrous oxide." *Titan I Ego Splavy.*, 2, pp. 152–157.

Wechsler, B. A., 1977, "Cation distribution and high-temperature crystal chemistry of armalcolite." *American Mineralogist*, 62, pp. 913–920.

Wechsler, B. A. and Prewitt, C. T., 1984, "Crystal structure of ilmenite ($FeTiO_3$) at high temperature and high pressure." *American Mineralogist*, 69, pp. 176–185.

Yang, H. and Hazen, R. M., 1999, "Comparative high-pressure crystal chemistry of karrooite, $MgTi_2O_5$, with different ordering states." *American Mineralogist*, 84, pp. 130–137.